Density Functional Tight Binding Study of Structural Dynamics in Functional Materials

機能性材料における構造ダイナミクスに関する密度汎関数強結合法による研究

Taku Hayashi

Department of Chemistry, Graduate School of Science

Nagoya University

2021

Contents

1. General Introduction

Today various functional materials have been applied throughout our life and industry. These materials can be classified to two types, materials with static functions and materials with dynamic functions. The former makes use of static properties of the materials, such as electronic properties and porosity, while the latter utilizes dynamic properties of the materials, such as structural changes in response to external stimuli and ion conductions.[1-3] Dynamics of atoms and molecules often plays key roles on such dynamic functions. Therefore, understanding of the roles of the dynamics of atoms, molecules and ions of the functions will tell us which factor is particularly important for the functions and help us choosing the components of materials to express greater functions, which is important for new design and further development of functional materials. In addition to experimental investigations of such dynamics, theoretical calculations have been performed to elucidate dynamics of functions at atomic and molecular levels at time scales of ps or shorter and to examine various conditions including those that are difficult to obtain experimentally.

For example, in electrolytes of fuel cells, the dynamics of proton conduction plays an essential role on the function to deliver protons from anodes to cathodes, while preventing electrical contact of the electrodes.[4-7] Electrolytes with high proton and low electron conductivities, and high thermal and chemical stability are required for efficient power generation of the fuel cells. Revealing the mechanisms of proton conduction in the candidates of electrolytes could enable us to develop new electrolytes which are distinct from the electrolytes currently in practical use and shows higher performances with lower costs. In this context, in addition to the experimental investigation of dynamics of

molecules and ions in the electrolytes,[8-10] various theoretical calculations such as molecular dynamics (MD) simulations and Monte Carlo simulations have been performed to elucidate the proton conduction mechanisms based on the dynamics from atomic levels to mesoscales, which can simulate dynamics of atoms and molecules that are difficult to observe directly in experiments.[2,3,11,12] Indeed, based on the proton conduction mechanisms, new electrolytes with greater functions than existing ones have been developed.[13]

MD method is one of the most popular computational methods to obtain dynamics of atoms and molecules.[14] In MD method, the atoms usually move based on the Newton equation, and time courses of the coordinates and velocities of the atoms can be obtained.[15] The word "MD" often refers to classical MD, where the attractive/repulsive forces between atoms are determined by empirical force fields partially estimated by computationally costly quantum chemical calculations. Since classical MD does not require the quantum chemical calculations during simulations, the computational cost of MD is considerably small, and therefore it is widely used especially for calculations of dynamics of large systems such as biomolecules. On the other hand, the computational accuracy of MD strongly depends on the quality of the force fields, and it is difficult to investigate dynamics of chemical reactions because force field is usually designed at the structures near to the minima of potential curves.

Another category of MD is *ab initio* MD (AIMD) simulation, where the force between atoms is determined by quantum chemical calculations during simulations.[14,16] Although in principle the accurate forces can be obtained by solving Schrödinger equations of the systems, it is impossible to solve them exactly for chemical systems. To overcome this difficulty and apply quantum mechanics to chemistry, various approaches such as

Hartree-Fock (HF) method, post HF theories, coupled cluster theory, and density-functional theory (DFT) method have been developed. In particular, DFT is a method to treat physical properties of the system such as energy as functionals of electron density, which is practical quantum chemical computational method because of reliable chemical accuracy and lower computational cost compared with other quantum chemical methods.[17,18] AIMD using DFT to calculate forces shows reliable accuracy and can describe bond cleavage and formation, and therefore is applicable for calculations to investigate dynamics of chemical reactions of small systems. However, the computational cost of AIMD is much higher than classical MD, which makes it difficult to investigate dynamics of large systems with AIMD.

A computational method that can compute dynamics of systems containing hundreds of atoms where chemical reactions can take place is required in order to investigate functions originating from their dynamics. In this thesis, density-functional tight-binding (DFTB) method, which is a semi-empirical approximation of DFT, is used for calculation of the force in MD simulations.[19-21] To obtain the time course of the dynamics of systems, an MD simulation using DFTB (DFTB-MD) repeats the process that the force working on atoms are computed with DFTB, Newton's equations of motion are solved using the force, and the coordinates and velocities of the atoms after a selected time step are calculated. DFTB is 100 to 1000 times faster than DFT and shows enough chemical accuracy for MD simulations with bond cleavage and/or formation.[22,23]

The theoretical backgrounds of DFTB are explained here briefly. In DFTB, the electron density $\rho(\boldsymbol{r})$, where $\boldsymbol{r}$ is the coordinate vector, is substituted by the sum of the reference density $\rho_0(\boldsymbol{r})$, determined by the neutral atomic densities, and the deviation $\delta\rho(\boldsymbol{r})$. Using this substitution, the Taylor series expansion of the total energy functional is performed.

The total energy, E, is written as Eq. (1),

$$\begin{aligned} E = \sum_{i}^{\mathrm{occ}} \langle \Psi_i | \hat{H}_0 | \Psi_i \rangle - \frac{1}{2} \int \int' \frac{\rho_0' \rho_0}{|\boldsymbol{r} - \boldsymbol{r}'|} - \int V_{XC}[\rho_0] \rho_0 + E_{ion} \\ + E_{XC}[\rho_0] \\ + \frac{1}{2} \int \int' \left(\frac{1}{|\boldsymbol{r} - \boldsymbol{r}'|} + \left. \frac{\delta^2 E_{XC}}{\delta \rho \delta \rho'} \right|_{\rho_0, \rho_0'} \right) \delta\rho \delta\rho' \\ + \frac{1}{6} \int \int' \int'' \left. \frac{\delta^3 E_{XC}}{\delta \rho \delta \rho' \delta \rho''} \right|_{\rho_0, \rho_0', \rho_0''} \delta\rho \delta\rho' \delta\rho'' + \cdots. \end{aligned} \tag{1}$$

Here, we denoted $\int = \int d^3r$, $\int' = \int d^3r'$, $\int'' = \int d^3r''$, $\rho = \rho(\boldsymbol{r}), \rho' = \rho(\boldsymbol{r}'), \rho'' = \rho(\boldsymbol{r}'')$. $\hat{H}_0$ is the Hamiltonian operator of the reference density and Ψ_i's are the Kohn-Sham wavefunctions. E_{ion} is the repulsion energy between nuclei. E_{XC} and V_{XC} are the exchange-correlation energy and potential, respectively.

Eq. (1) can be written down in a simple form as Eq. (2),

$$E = E_{\mathrm{H0}} + E_{\mathrm{rep}} + E_{\mathrm{2nd}} + E_{\mathrm{3rd}}. \tag{2}$$

Here E_{H0} is orbital energy depending on the reference density, corresponding to the first term of Eq. (1). E_{rep} corresponds to the second to fifth terms of Eq. (1), showing the contributions of repulsive energies. E_{2nd} and E_{3rd} are the second and third order term of the Taylor series expansions, corresponding to the sixth and seventh terms of Eq. (1), respectively. The terms with higher orders of the expansion were neglected.

In the DFTB method, several approximations are performed to decrease computational costs. First, the reference density ρ_0 is introduced and the wavefunction Ψ is approximated by the linear combination of atomic orbitals (LCAO). The LCAO coefficients c_{vi} are obtained by solving the secular equations shown in Eq. (3).

$$\sum_{\nu}^{N} c_{\nu i}\left(H_{\mu\nu}^{0} - \varepsilon_i S_{\mu\nu}\right) = 0. \quad (3)$$

Here $H_{\mu\nu}{}^{0}$ is the Hamilton matrix element and $S_{\mu\nu}$ is the overlap matrix element. Both $H_{\mu\nu}{}^{0}$ and $S_{\mu\nu}$ can be computed in advance, which means that no integral calculations are required during calculation of target systems. In addition, the minimal valence basis sets are used to decrease computational costs. The resulting E_{H0} is expressed as Eq. (4),

$$E_{\mathrm{H0}} = \sum_{iab}\sum_{\mu\in a}\sum_{\nu\in b} n_i\, c_{\mu i} c_{\nu i} H_{\mu\nu}^{0}, \quad (4)$$

where n_i is the occupation number of the ith molecular orbital.

Second, E_{rep} is approximated by the repulsive two-center potentials V^{rep} as Eq. (5),

$$E_{\mathrm{rep}} \approx \frac{1}{2}\sum_{ab} V_{ab}^{\mathrm{rep}}[\rho_a^0, \rho_b^0, r_{ab}], \quad (5)$$

where r_{ab} is the distance between atom a and atom b.

Third, E_{2nd} is approximated as Eq. (6),

$$E_{\mathrm{2nd}} \approx \frac{1}{2}\sum_{ab} \Delta q_a \Delta q_b \gamma_{ab}, \quad (6)$$

where Δq_a is the charge of atom a, and γ is the function explaining the electron-electron interaction.

Finally, E_{3rd} is approximated by the similar approximation to E_{2nd} as Eq. (7),

$$E_{\mathrm{3rd}} \approx \frac{1}{3}\sum_{ab} \Delta q_a^2 \Delta q_b \Gamma_{ab}, \quad (7)$$

where $\Gamma_{ab} = \left.\frac{\partial \gamma_{ab}}{\partial q_a}\right|_{q_a^0}$; q_a^0 is the neutral atomic charge of atom a.

There are two types of the popularly used DFTB methods, the second order DFTB or the self-consistent charge DFTB (SCC-DFTB) and the third order DFTB or DFTB3. The

former includes the Taylor series expansion up to the second order, while the latter includes up to the third order. The total energies of SCC-DFTB and DFTB3 are expressed as Eqs. (8) and (9), respectively.

$$E_{\mathrm{SCC-DFTB}} = \sum_{iab}\sum_{\mu\in a}\sum_{\nu\in b} n_i\, c_{\mu i}c_{\nu i}H^0_{\mu\nu} + \frac{1}{2}\sum_{ab} V^{\mathrm{rep}}_{ab}[\rho^0_a, \rho^0_b, r_{ab}] + \frac{1}{2}\sum_{ab}\Delta q_a \Delta q_b \gamma_{ab}. \tag{8}$$

$$E_{\mathrm{DFTB3}} = \sum_{iab}\sum_{\mu\in a}\sum_{\nu\in b} n_i\, c_{\mu i}c_{\nu i}H^0_{\mu\nu} + \frac{1}{2}\sum_{ab} V^{\mathrm{rep}}_{ab}[\rho^0_a, \rho^0_b, r_{ab}] + \frac{1}{2}\sum_{ab}\Delta q_a \Delta q_b \gamma_{ab} + \frac{1}{3}\sum_{ab}\Delta q_a^2 \Delta q_b \Gamma_{ab}. \tag{9}$$

Because of these approximations, DFTB is much faster than DFT, and DFTB-MD is much faster than AIMD with DFT. It should be noted that DFTB is not actually an *ab initio* method because it uses empirical parameters.[24] For efficient and accurate calculations with DFTB, we should develop or choose appropriate parameters. In addition, descriptions of noncovalent interactions such as London dispersion and hydrogen bonds in DFTB tend to be insufficient, and some empirical corrections are required to investigate dynamics on which such noncovalent interactions play key roles.

The purpose of this thesis is to reveal dynamics of various functional materials with theoretical calculations, mainly DFTB-MD simulations, and elucidate the mechanisms of the functions of the materials based on the dynamics, in particular helix-inversion of a double-helical molecule, self-assembly of a covalent organic framework (COF), and proton conduction of a one-dimensional (1D) coordination polymer (CP).

The contents of this thesis are shown below. First the theoretical backgrounds of DFTB and the advantages and points to note of DFTB have been described in this section

(Section 1).

Sections 2 to 4 describe dynamics of specific functional materials and its effects on the functions of the materials. In Section 2, local dynamics of single molecules and correlations between them are investigated. As a representative of local dynamics of a single molecule, the helix-inversion dynamics of a double-helical molecule is focused and the expression mechanism of the helix-inversion function are discussed. Attracted by the essential functions of double-helical biopolymers represented by DNA in biological systems,[25,26] many researchers have synthesized various artificial double-helical oligomers and polymers.[1,27] Recently a double-stranded helical oligomer covalently bridged by cyclic boronate ester units named BBDD was synthesized, which undergoes helix-inversion that might be useful as a platform to design molecular rotors.[28] However, the details of the mechanism of helix-inversion could not be investigated in the experiments. In this section, DFTB-MD simulations of BBDD are performed to reveal dynamics of conformational changes including helix-inversion. The importance of disentanglement and exchange of the twisted terminal trimethylsilyl (TMS) groups on the helix-inversion is reported. The potential of mean force (PMF) profiles confirm that the originally supposed "concurrent" rotation of the boronate esters and the helix-inversion includes "stepwise" processes in shorter time scales, triggered by the disentanglement and exchange of the TMS groups. These results indicate controllability of inversion dynamics of double-helical molecules such as BBDD by tuning of the terminal groups.

Not only local structures and dynamics of molecules discussed in Section 2 but also global structures and dynamics are important for functions, especially in periodic compounds. Section 3 focuses on a COF, which is an example of materials whose global structure plays important roles on the functions, and discusses the formation mechanisms

of the global structures from the optimized geometries. COFs are crystalline porous materials in which organic molecules connect via covalent bonds to form periodic structures, which shows various functions based on the global structures such as gas adsorption.[29-31] However, it is difficult to obtain their structures experimentally due to low crystallinity of COFs, even though they possess periodical structures.[32-34] In this section, geometry optimization of various stacked structures of a double-stage two-dimensional (2D) COF using DFTB method are performed to compare energetic stabilities of the optimized structures and to discuss that what kind of the structures are the most likely in the actual systems. The result shows that rotations of *p*-phenylene rings, which can occur commonly in monolayers, greatly affect the global stacking order. Here the discrepancy between the powder X-ray diffraction (XRD) pattern estimated from the most stable optimized structure and that experimentally observed is also discussed. The discrepancy indicates the importance of dynamics in the self-assembly process of the organic components of the COF.

Compared with single organic molecules discussed in Section 2 and COFs composed by assembly of organic molecules discussed in Section 3, in which the charges distribute relatively uniformly because the structures of those materials are formed by covalent bonds, coordination compounds containing metal ions could show effects of localized charges on dynamics and function expression mechanisms. Section 4 focuses on a 1D CP composed of zinc ions bridged by phosphate linkers and imidazolium cations (ImH_2^+), which shows proton conductivity in anhydrous conditions and is potentially applicable to new electrolytes of fuel cells, and investigates the dynamics and mechanisms of the proton conduction of the CP.[35] The accelerated dynamics of ImH_2^+ is expected to promote the nonlinear increase of the conductivity in the CP around 55 °C. However, the proton

conduction mechanisms and pathways of the CP have not been revealed well. The DFT calculation from the static point of view showed that the change of the ImH_2^+ orientation have influence on the stability of the system through the hydrogen-bonding stabilizations. The DFTB-MD simulations showed that the dynamics of the ImH_2^+ is not free rotation but stepwise orientation change. These results suggest that the ImH_2^+ contributes to the stabilization of the system by hydrogen bonds rather than rotates dynamically. On the other hand, proton transfer reactions are observed only between the phosphate groups and ImH_2^+ ions are not involved in the proton transfer reactions during the DFTB-MD simulations, due to the lower acidities of ImH_2^+ than phosphate groups. This indicate that the proton conduction pathways are on the phosphate groups rather than the ImH_2^+ groups.

Finally, in Section 5 the general conclusions and future outlooks are described.

2. Dynamics of a Double-helical Molecule

2.1. Introduction

DNA has a double-helical structure, which plays essential regulatory roles in biological systems.[25,26] The structure has tempted researchers to design and synthesize a variety of artificial double-stranded helical oligomers and polymers because double-helical materials which imitate structure-dependent functions of DNA represented by information storage and capability to replicate itself will be utilized for various applications such as data storage devices.[1,27,36-45] It has been revealed that some of synthetic double-stranded helices could imitate such structure-dependent functions of DNA.[1,26,43] DNA can cause structural change from the right-handed helix to the left-handed helix, and similar to that, some synthetic double-helical molecules have been shown to cause helix-inversion by introduction of external physical or chemical stimuli such as solvent polarity, temperature change, and the coordination of side chains of the helix to metal ions.[40,41,44-46] Such "inverting molecules" are potentially applicable to asymmetric catalysts or fluorescence switching sensors.[40,41] Compared with invertible single-helical molecules, which are both abundant and well-studied, the number of molecules with invertible double-helical structures is still limited, thus the understanding of the helix-inversion in double-helical structures, in particular those linked by covalent bonds, is also limited.[1,27,47-51] Some insights of helix-inversion mechanisms have been reported for triple-stranded helicates linked by dissociative coordination bonds.[52-54] However, helical structures bridged covalently show helix-inversion without bond dissociation. Therefore, having the controllability of the dynamics of inversion is important to design functional double-helices utilizing inversion for practical applications.

Recently, Yashima et al. have synthesized a double-helical molecule consisting of a m-terphenylene-ethynylene-based strand which has two boronate groups (BB) and another m-terphenylene-ethynylene-based strand which has two diol groups (DD), connected via covalent bonds of the boronate groups and diol groups, named BBDD (Figure 2.1(a)).[28] Because cyclic boronate esters bridging the strands covalently are stable in organic solvents, BBDD is also stable. The ends of the strands are capped by trimethylsilyl (TMS) groups, twisting around the strands. In the BBDD system, "concurrent" rotation of the cyclic boronate ester linkers and the helix-inversion was speculated. The nature of these conformational changes, however, has not been clarified. It is expected that time-resolved understanding these dynamic processes at the atomic level will contribute to the design of new external stimuli responsive functional double-helical structures.

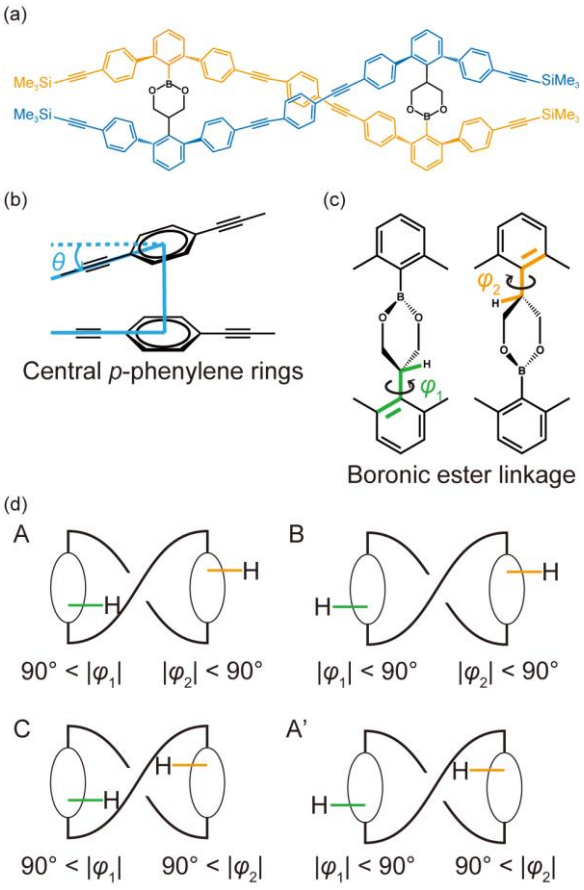

Figure 2.1. (a) Schematic structure of BBDD. (b) The definition of dihedral angle, θ. (c) The definitions of dihedral angles, φ_1 and φ_2. (d) Schematic description of conformations A, A', B, and C determined by the orientations of H.

In this section, elucidation of the dynamics of conformational changes in BBDD and their correlations using MD simulations with the SCC-DFTB method is explained, as an example of investigations of local dynamics of single molecules affecting mechanisms of functions.[19] The focused dynamics of BBDD is the conformational changes of the helix-inversion, the rotation of the cyclic boronate ester linkers, and the disentanglement and exchange of the relative positions of the terminal TMS groups. From the simulations, the importance of the disentanglement and sequential exchange of the TMS groups on the helix-inversion has been found. Analysis of potential of mean force (PMF) plots revealed that the exchange decreased the energy barrier of the inversion dramatically. The results indicate that the helix-inversion process would require the exchange of the TMS groups as the initial step.

2.2. Computational Methods

2.2.1. Details of calculations

Three different conformations of the left-handed helical geometries of BBDD corresponding to A, B and C conformations defined by the directions of the cyclic boronate esters, φ_1 and φ_2 as shown in Figure 2.1(d), were optimized. Each optimized conformation is named BBDD-A, BBDD-B and BBDD-C, respectively. All optimization was performed using DFT with the resolution of identity approximation implemented in the TURBOMOLE package version 6.6.[55,56] TPSS exchange-correlation functional and

def-SV(P) basis set were applied to all atoms[56-60] with Grimme D3 dispersion corrections.[64]

The three geometries were re-optimized using SCC-DFTB implemented in the DFTB+ program package version 1.2.2 to investigate the dynamics of BBDD.[19,61] The matsci-0-3 Slater-Koster parameters were employed throughout the section.[62,63] Lennard-Jones type dispersion correction with the universal force field (UFF) parameters was included.[64,65] In this section, the SCC-DFTB with the UFF dispersion correction is abbreviated as DFTB, and MD with DFTB is abbreviated as DFTB-MD.

DFTB-MD simulations were performed using the re-optimized BBDD-A, BBDD-B and BBDD-C structures as the initial structures. Each name of the initial structure is also used as the name of each trajectory. All DFTB-MD simulations were run for 400 ps with a time interval of 0.4 fs using the Nosé-Hoover NVT ensemble at 1000 K. 8 fs MD snapshots were collected to investigate conformational dynamics of BBDD. The geometries of every 200 fs were optimized with DFTB for the analysis of essential changes of the different structures and energies.

2.2.2. Definition of angles

For structural analysis, dihedral angular parameters, θ, φ_1 and φ_2 shown in Figure 2.1 were defined to classify different structural conformations. Change of the sign of the dihedral angle, θ, defined by the two central *p*-phenylene rings, is equivalent to the helix-inversion. Because change of the sign of the dihedral angles, φ_1 and φ_2, corresponds to the rotation of cyclic boronate ester linkers, φ_1 and φ_2 define A, A', B and C conformations. Other dihedral angular parameters, λ_1 and λ_2, formed by the two TMS groups at the left and right ends of the helix were defined as Figure 2.2(d) respectively, to analyze the exchange processes of the terminal TMS groups. Conformations having a

TMS group and the central p-phenylene ring in a strand located on the same side (i.e. $\lambda \times \theta < 0$) and on the opposite side (i.e. $0 < \lambda \times \theta$) are denoted as parallel (**P**) and helical (**H**), respectively. Therefore, all optimized geometries were classified with conditions ($0 < \lambda_1 \times \theta$ and $0 < \lambda_2 \times \theta$) as [**H**, **H**], ($\lambda_1 \times \theta < 0$ and $\lambda_2 \times \theta < 0$) as [**P**, **P**], and ($0 < \lambda_1 \times \theta$ and $\lambda_2 \times \theta < 0$ or $\lambda_1 \times \theta < 0$ and $0 < \lambda_2 \times \theta$) as [**H**, **P**] or [**P**, **H**], respectively, as shown in Figure 2.2. The ratio of the number of geometries showing each conformation to the total and the mean energy of each conformation were also calculated.

2.2.3. PMF profiles

PMF profiles were plotted using the weighted histogram analysis method (WHAM) program package ver. 2.0.9 from structures and potential energies collected from the three DFTB-MD trajectories.[66,67] 1D PMF profiles as functions of θ, φ_1 and φ_2 and a 2D PMF profile as a function of λ' ($= \lambda_1 + \lambda_2$) and θ were plotted. To reveal the correlation between helix-inversion and the exchange of TMS groups, 1D PMF profiles as functions of θ using structures with the ranges of $\lambda' < -40°$, $-40° < \lambda' < 40°$ and $40° < \lambda'$, and 1D PMF profiles as functions of λ' using the structures with the ranges of $\theta < 0°$and $0° < \theta$ were plotted.

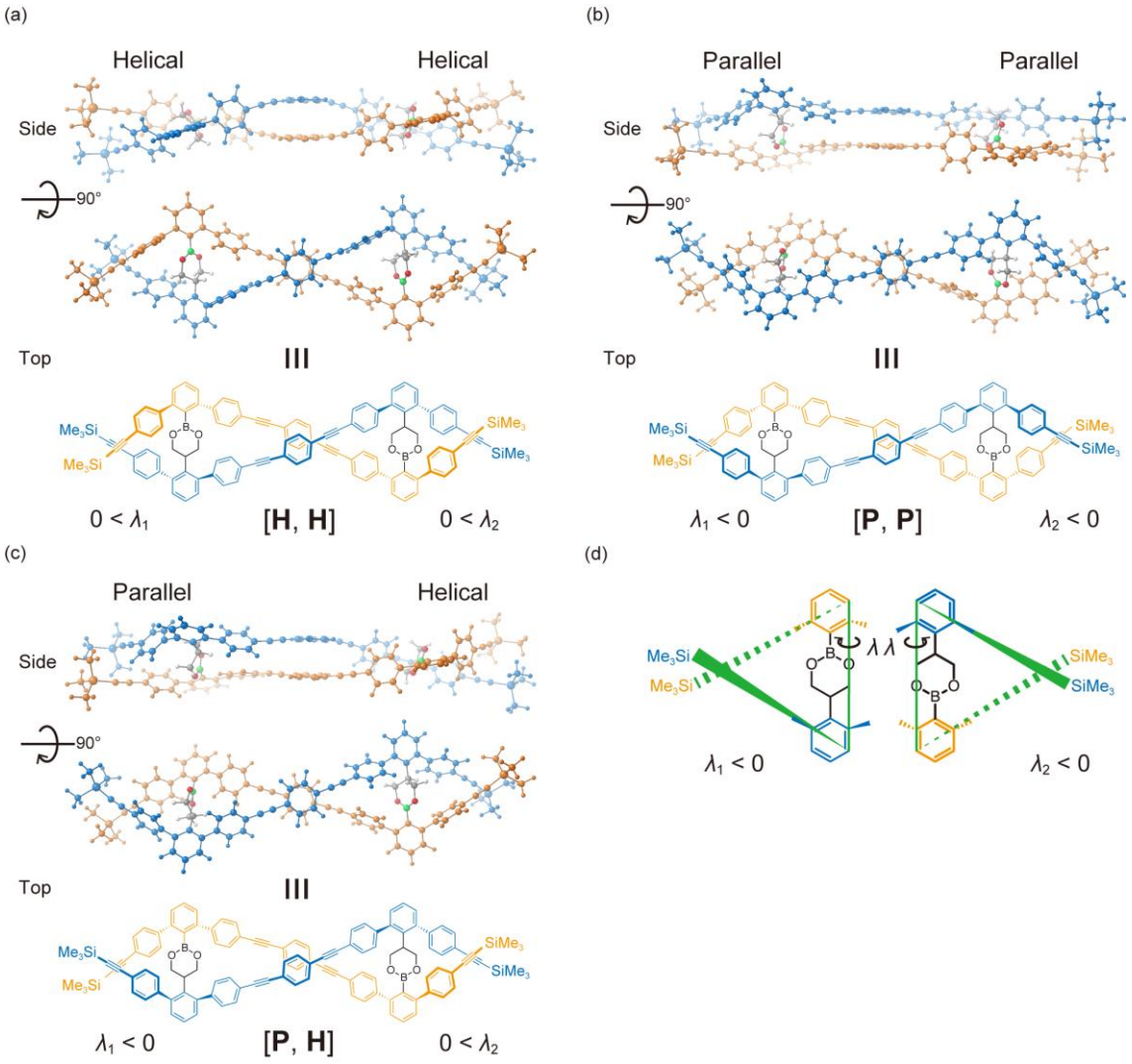

Figure 2.2. (a) to (c) Side views and top views of **H** and **P** conformations. (d) Definition of the λ (referring to λ_1 or λ_2).

2.3. Results and Discussions

The geometries of BBDD optimized with DFTB are shown in Figure 2.3. The relative energies of the optimized geometries with DFTB and DFT are summarized in Table 2.1.[28] The orders of the relative stabilities of the optimized geometries with DFTB and DFT are same, BBDD-B < BBDD-A < BBDD-C. In the most stable structure, BBDD-C, the H atoms in the boronate ester linker on both ends illustrated in Figure 2.1(c) are oriented

"inward" with φ = 166.0°. On the contrary, the H atoms are oriented "outward" with φ = 1.2° in the least stable BBDD-B structure. The relative stability of BBDD appears to be determined by the orientation of the H atoms on the boronate ester linkers. The rotational motion of the *p*-phenylene group at the outer chain of the DD strand might decrease steric repulsion between neighbor H atoms in the *p*-phenylene group and the adjacent benzene ring, which could be interfered by the presence of the H atom oriented "outward", which would destabilize BBDD. Indeed, in BBDD-A, where the H atom on one end is oriented "inward" with φ = 165.8° and the H atom on the opposing end is oriented "outward" with φ = 2.2°, the stability of the structure is intermediate. Because both DFT and DFTB showed the same trend of stability depending on the structural features, after this results obtained from DFTB calculations are discussed, with regards to conformational change and dynamics of BBDD.

Table 2.1. Relative energies of each conformation to BBDD-C in kcal mol^{-1} unit.

	TPSS+D / def-SV(P)	DFTB / matsci-0-3
BBDD-A	4.85	1.72
BBDD-B	6.04	5.22
BBDD-C	0	0

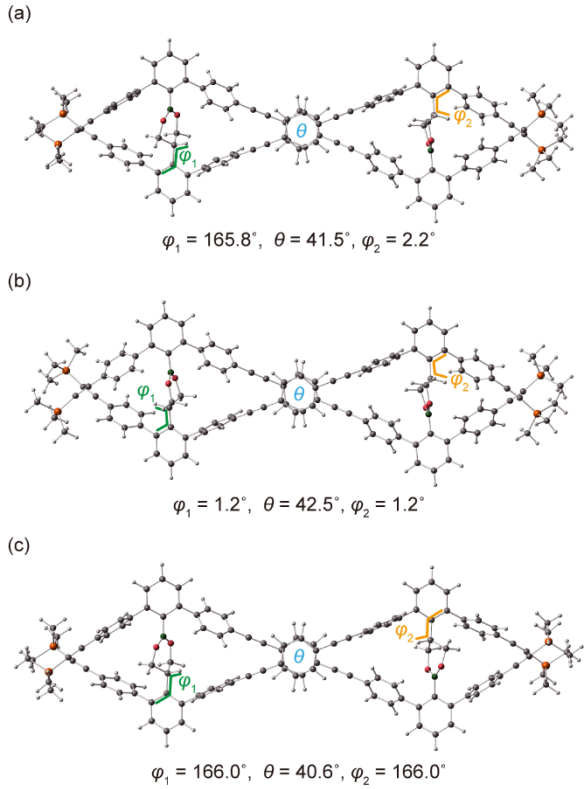

Figure 2.3. Optimized structures of (a) BBDD-A, (b) BBDD-B, and (c) BBDD-C by DFTB. Gray, white, red, green, and orange spheres indicate C, H, O, B and Si atoms, respectively.

To examine synchronicity of the helix-inversion and the rotation of the boronate ester linkers, the angles of θ, $|\varphi_1|$, and $|\varphi_2|$ and the relative energies over time from the DFTB-MD trajectories were plotted in Figure 2.4. Although changes in $|\varphi|$ alternating above and below $|\varphi| = 90°$ indicating changes of the orientations of the boronate ester linkers, and change of the sign of θ suggesting helix-inversion were found, it is almost impossible to discuss the frequency and timing of synchronous conformational changes because distinguishing the angle changes corresponding to the essential conformational changes and the thermal fluctuation of the angles, in particular for θ, is difficult. To interpret substantial dynamics by excluding geometric fluctuation, BBDD geometries at every 200

fs were optimized and their angles of θ, $|\varphi_1|$, and $|\varphi_2|$ as well as their relative energies over time were plotted in Figure 2.5. From these geometries, 32 times of helix-inversion and only 8 times of the rotation of the boronate ester linkers in total among all trajectories were observed as summarized in Table 2.2. The frequency of the former was quite higher than that of the latter, thus the synchronous conformational changes suggested experimentally within the time scale of the simulations were not found. The helix-inversion and the rotation of the boronate ester linkers were observed, each of which is a process that occurs in much shorter time scales than the originally supposed "concurrent" conformational changes, although correlation between the helix-inversion and the rotation were not observed.

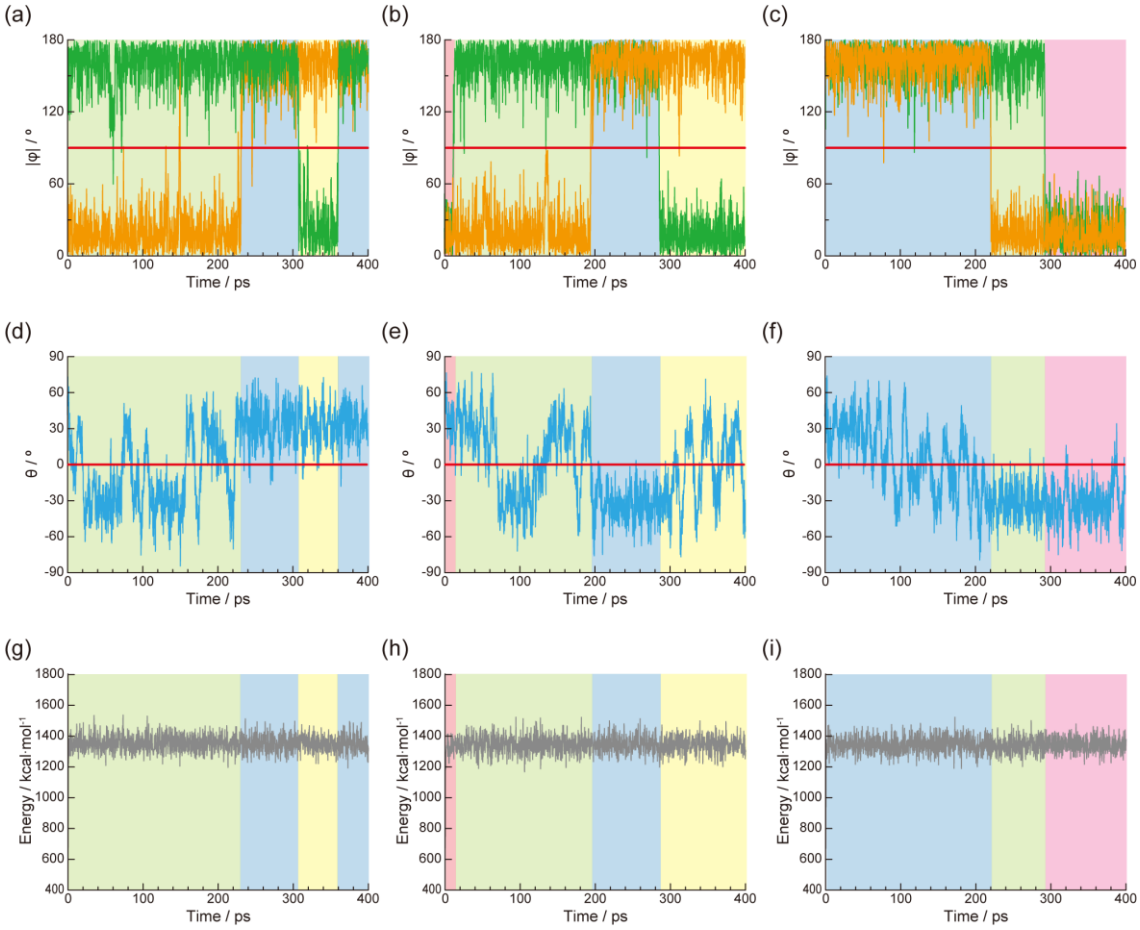

Figure 2.4. (a) to (c) $|\varphi_1|$ (green) and $|\varphi_2|$ (orange), and (d) to (f) θ of every 8 fs MD frames for 400 ps. (g) to (i) relative energies to the lowest energy among all optimized geometries. The data of (a), (d), and (g) were obtained from the MD trajectory of BBDD-A, as well as (b), (e), and (h) from BBDD-B, and (c), (f), and (i) from BBDD-C. Light green, yellow, red, and blue colors on background indicate A, A', B, and C conformations determined by the optimized geometries plotted in Figure 2.5, respectively.

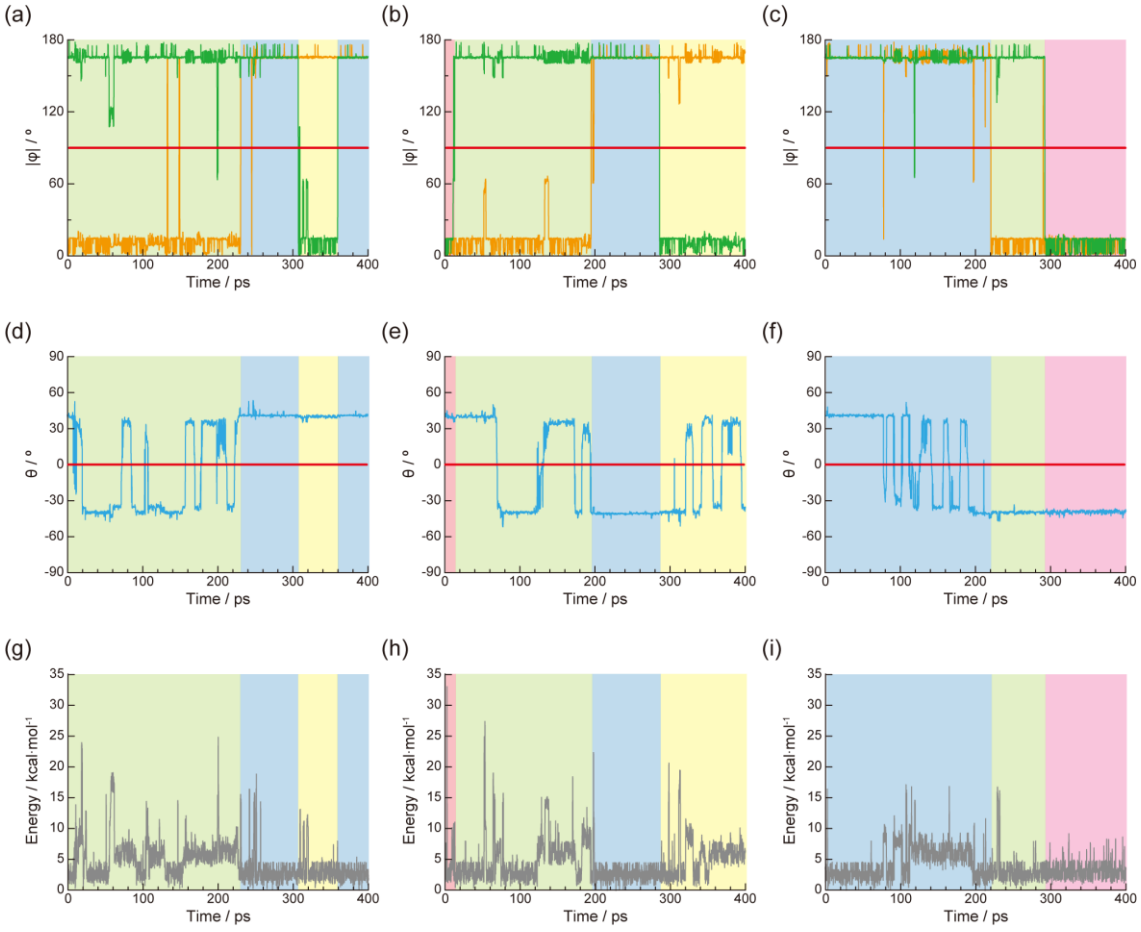

Figure 2.5. (a) to (c) $|\varphi_1|$ (green) and $|\varphi_2|$ (orange), and (d) to (f) θ of optimized geometries obtained from every 200 fs MD frames for 400 ps. (g) to (i) relative energies to the lowest energy among all optimized geometries of all MD frames. The data of (a), (d), and (g) were obtained from the MD trajectory of BBDD-A, as well as (b), (e), and (h) from

BBDD-B, and (c), (f), and (i) from BBDD-C. Light green, yellow, red, and blue colors on background indicate A, A', B, and C conformations determined by φ without considering φ changes like spikes, respectively.

Table 2.2. The numbers of rotation of the boronate ester linkers at left and right ends, and the number of helix-inversion.[a]

	Rotation (left)	Rotation (right)	Helix-inversion
BBDD-A	2	1	10
BBDD-B	2	1	11
BBDD-C	1	1	11
Total	5	3	32

[a]Momentary conformational changes shorter than 2 ps were excluded from counting.

A more detailed analysis of relative energy plots in Figure 2.5(g) to (i) revealed three clear energy ranges of local minima between 0 to 5 kcal mol^{-1} (low energy), 5 to 8 kcal mol^{-1} (medium energy), and 8 to 10 kcal mol^{-1} (high energy). Further investigation of the geometries at these three energy levels by introducing λ_1 and λ_2 proposes that the energy levels are determined by the conformations of the terminal TMS groups in BBDD. As displayed in the first 2 ps of the Supporting Movie, the disentanglement of the "twist conformation" of the two TMS groups occurred to form an unraveled conformation, followed by an exchange of relative positions of the TMS side chains. This process is equivalent to changes from **H** to **P** conformation or from **P** to **H** conformation as

illustrated in Figure 2.2. To understand more deeply the correlations among the disentanglement and exchange of the terminal TMS groups, the helix-inversion, and the distinct energy levels, the angles of λ_1, λ_2, and θ and the relative energies of the optimized geometries over time were plotted in Figure 2.6. The conformation where the signs for all λ_1, λ_2 and θ are the same corresponds to the [**H**, **H**] conformation ($0 < \lambda_1 \times \theta$ and $0 < \lambda_2 \times \theta$), while the other conformations correspond to the [**P**, **H**] ($\lambda_1 \times \theta < 0$ and $0 < \lambda_2 \times \theta$), [**H**, **P**] ($0 < \lambda_1 \times \theta$ and $\lambda_2 \times \theta < 0$), and [**P**, **P**] ($\lambda_1 \times \theta < 0$ and $\lambda_2 \times \theta < 0$) conformations. The sign change of λ_2 means the exchange of TMS groups on the right end, corresponding to the conformational change from [**H**, **H**] to [**H**, **P**] (e.g. at 68 ps in BBDD-B) and [**P**, **H**] to [**P**, **P**] (e.g. at 14 ps in BBDD-A), and their reverse processes, as shown by the sign change of the product of $\lambda_2 \times \theta$. This is similar for the sign change of λ_1 corresponding to the exchange of TMS groups on the left end. The sign change of θ means the helix-inversion, corresponding to the conformational change from [**H**, **H**] to [**P**, **P**] (e.g. at 182 ps in BBDD-B) and [**H**, **P**] to [**P**, **H**] (e.g. at 69 ps in BBDD-B), and vice versa, as shown by the sign changes of the both products of $\lambda_1 \times \theta$ and $\lambda_2 \times \theta$. Hereafter, both [**H**, **P**] and [**P**, **H**] are denoted as [**H**, **P**] since they are mirror images of one another and keeping the essentially same conformations. The evaluated average energies of [**H**, **H**] (3.2 kcal mol^{-1}), [**H**, **P**] (6.5 kcal mol^{-1}) and [**P**, **P**] conformations (9.1 kcal mol^{-1}) correspond to the abundance ratios of 67.9 %, 27.4 %, and 4.7 % of the total of the three trajectories respectively, and correspond well to the low, medium and high energy levels respectively in Figure 2.5(g) to (i). As a result, it is concluded that the relative stability of BBDD is determined by the conformation of the TMS groups, besides the orientation of the boronate ester linkers, as mentioned above. Furthermore, the total numbers of exchange following disentanglement of terminal TMS groups on each side and helix-inversion in

each trajectory, as well as the number of helix-inversion in each conformation of TMS groups, were summarized in Table 2.3, to unravel the process of the helix-inversion. The exchange of TMS groups was observed 21 times as a total of both sides, which was less than the number of helix-inversions (32 times). The [**H**, **P**] conformation showed a larger number of the helix-inversion with a smaller abundance ratio than the [**H**, **H**] conformation, meaning higher frequency of the helix-inversion. This indicates that the exchange of TMS groups increases the possibility of the helix-inversion. The [**P**, **P**] conformation showed the same number of the helix-inversion as [**H**, **H**] even with a much smaller abundance ratio than [**H**, **H**] and [**H**, **P**], indicating that the frequency of helix-inversion was very high. The result proposes that the exchange of TMS groups following their disentanglement is an important step to helix-inversion as an elemental dynamics in BBDD because the helix-inversion occurs more frequently when the conformation takes [**H**, **P**] and [**P**, **P**] conformations.

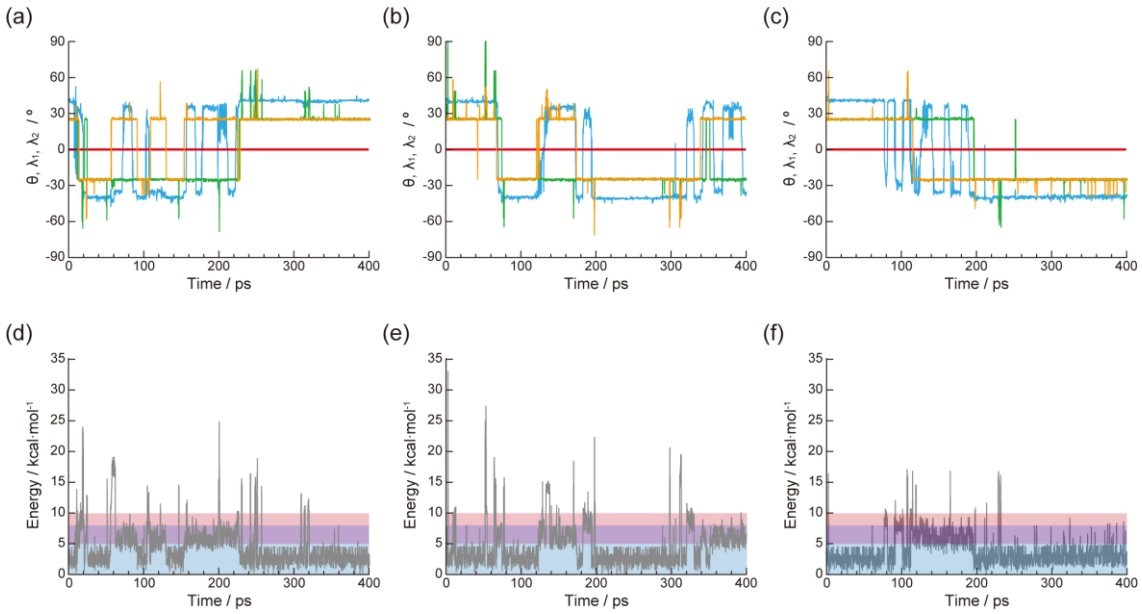

Figure 2.6. (a) to (c) dihedral angles of λ1 (green), λ2 (orange), and θ (blue) of optimized geometries obtained from every 200 fs MD frames. (d) to (f) relative energies to the lowest energy among all optimized geometries of all MD frames. Light blue, purple, and red colors on the background indicate the low, middle, and high energy levels, respectively. The data of (a) and (d) were obtained from the MD trajectory of BBDD-A, as well as (b) and (e) from BBDD-B, and (c) and (f) from BBDD-C.

Table 2.3. Numbers and frequencies of exchange of TMS groups for left and right ends and helix-inversion in total, and helix-inversion in each conformation of [**H**, **H**], [**H**, **P**], and [**P**, **P**].[a]

Trajectory	Exchange (left)	Exchange (right)	Helix-inversion in total	Helix-inversion in [**H**, **H**]	Helix-inversion in [**H**, **P**]	Helix-inversion in [**P**, **P**]
BBDD-A	4	8	10	1	7	2
BBDD-B	3	4	11	2	7	2
BBDD-C	1	1	11	3	6	2
Total	8	13	32	6	20	6
Frequency (ps-1)[b]	0.0067	0.011	0.027	0.0074	0.061	0.11

[a] Momentary conformational changes shorter than 2 ps were excluded from counting.

[b] Frequency = Number / (400 ps × number of trajectories × abundance ratio of the conformation), where number of trajectories is 3.

The dynamics of the conformational changes was delved from an energetic point of view using 1D and 2D PMF profiles. Plots of 1D PMF profiles of θ, φ_1 and φ_2 are shown in Figure 2.7. The energy barrier of θ around 0° is much smaller than those of φ_1 and φ_2 around ±90°, which agrees with the trends that the frequency of the helix-inversion is higher than that of the rotation of the boronate ester linkers. This shows that structural and energetic analyses are consistent. To investigate the energy barriers of the helix-inversion depending on the exchange of TMS groups, and the processes of the helix-inversion of the whole structure, a new parameter, $\lambda' = \lambda_1 + \lambda_2$ was defined for plotting a 2D PMF profile of λ' vs. θ as illustrated in Figure 2.8. Furthermore, the profile was divided into three regions of λ' corresponding to the conformations of TMS groups and their 1D PMF profiles of θ were plotted separately, i.e. $\lambda' < -40°$ for right-handed [**H**, **H**] or [**P**, **P**], $-40° < \lambda' < 40°$ for [**H**, **P**], and $40° < \lambda'$ for left-handed [**H**, **H**] or [**P**, **P**]. The energy barrier of the helix-inversion in [**H**, **P**] is much smaller than those of the other conformations, suggesting that helix-inversions are more likely to occur in this state. On the contrary, the energy barriers in [**H**, **H**] are much higher and [**P**, **P**] has no clear local minima, indicating that the helix-inversion in [**H**, **H**] are less likely to take place and the inverted [**P**, **P**] tends to return to [**H**, **H**]. Next the 2D PMF profile of θ was divided into $\theta < 0°$ (the right-handed helix) and $0° < \theta$ (the left-handed helix), and the 1D PMF profile of λ' was plotted for each region as shown in Figure 2.9 to examine the energy barriers of the process of exchange following the disentanglement of TMS groups between [**H**, **H**] and [**H**, **P**] conformations and between [**H**, **P**] and [**P**, **P**] conformations. The exchange from [**H**, **P**] to [**P**, **P**] needs more energy than to [**H**, **H**], indicating that [**H**, **P**] is more likely to alter to [**H**, **H**] than to [**P**, **P**] by the exchange. The resulting energy barriers obtained from the 1D PMF profiles of θ and λ' are consistent with the trend of frequencies

of the helix-inversion and the exchange of TMS groups described above. According to the 2D PMF profile, the helix-inversion processes seem to undergo the following set of steps: 1) the TMS groups at one end of BBDD disentangle to an unraveled conformation and then exchange their relative positions, 2) helix-inversion takes place passing through a low energy barrier, and 3) TMS groups at the other end disentangle and exchange, shown in the Figure 2.8(a). In the inverting process, bond dissociations of boronate esters are not necessary, and any bond dissociation were not observed during MD simulations at 1000 K. Therefore, the dissociation process of helix-inversion could be excluded because of the higher stability of the covalent bonds of the boronate ester bridges, compared with coordination bond generally. The result of this analysis proposes that the disentanglement and exchange dynamics in BBDD are the rate-determining processes of the dynamics of helix-inversion of BBDD because the energy barriers of them are much higher than that of helix-inversion itself.

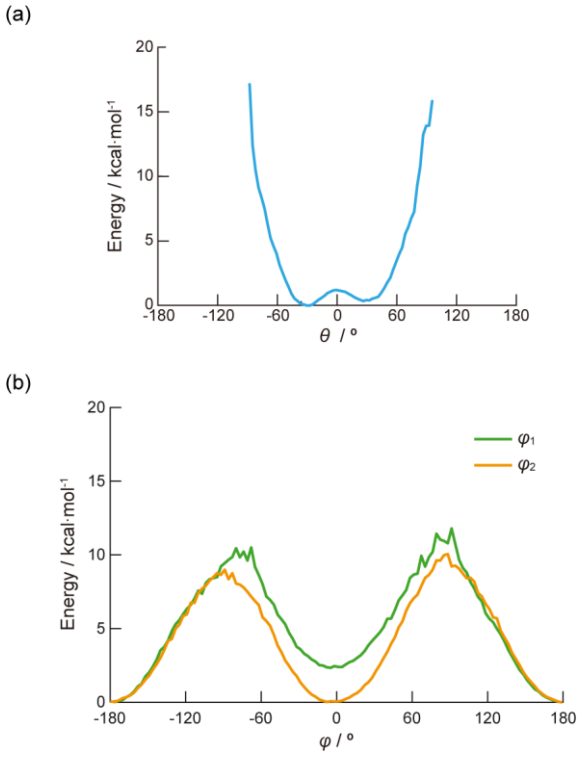

Figure 2.7. (a) plot of 1D PMF of θ. (b) plots of 1D PMF of φ_1 and φ_2. The bin width of the histograms is 3°.

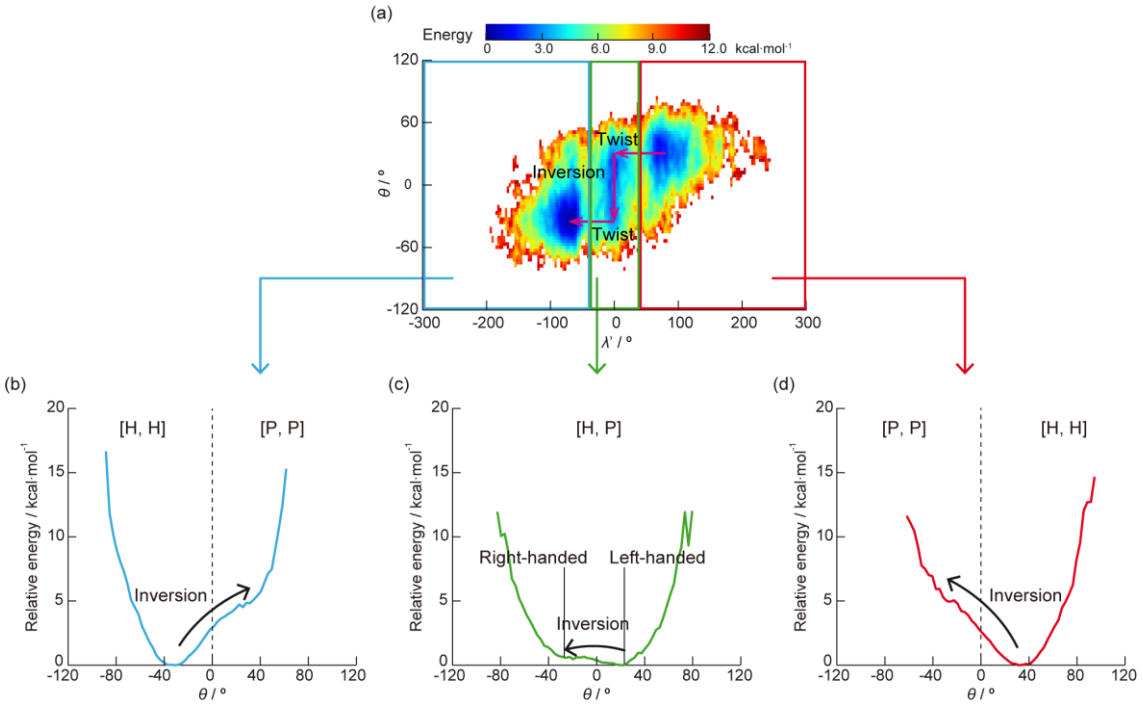

Figure 2.8. (a) plot of 2D PMF of λ' vs. θ. The pink arrows indicate the inverting processes. (b) to (d) relative energy plot of 1D PMF of θ using the structures with the ranges of λ' < -40° (blue), -40° < λ' < 40° (green), and 40° < λ' (red). The bin width of the histograms is 3° for all plots.

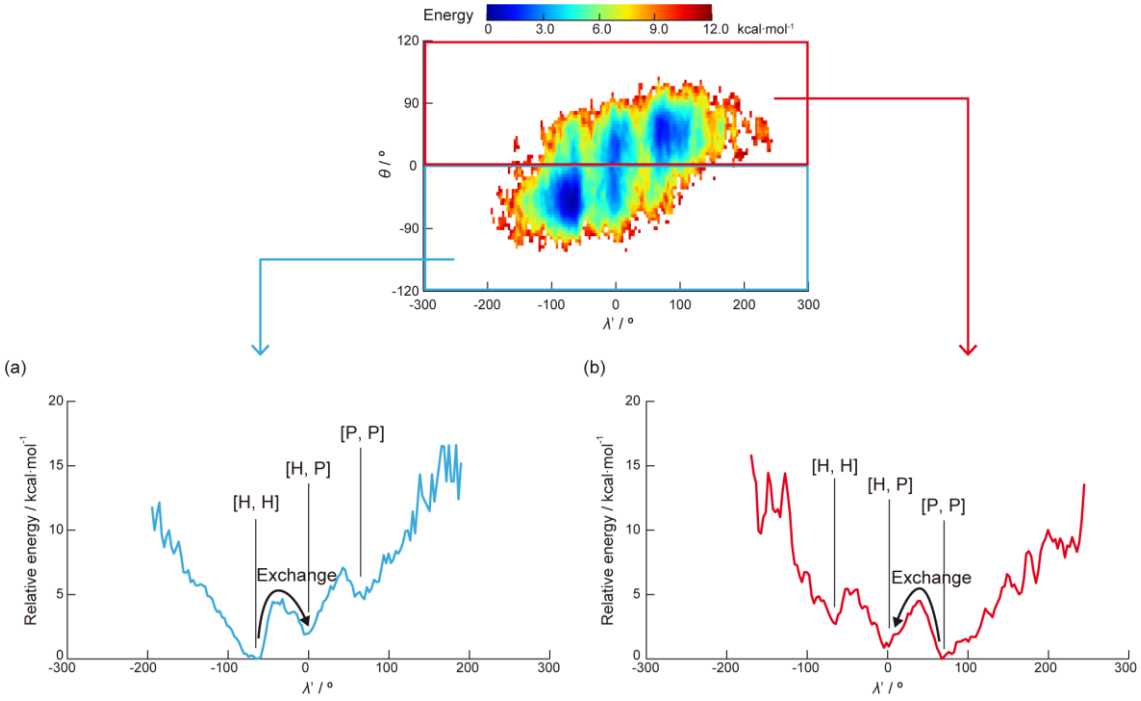

Figure 2.9. Relative energy plot of 1D PMF of λ' of (a) θ < 0°and (b) 0° < θ, corresponding to the right-handed and left-handed helices, respectively. The bin width of the histograms is 3°.

2.4. Conclusions

The dynamics of conformational changes found in the double-helical structure, BBDD, were theoretically examined using DFTB-MD. Although it has been observed that the rotation of the boronate ester linkers and helix-inversion are surely fundamental processes to the experimentally expected conformational change, clear evidence confirming synchronous or "concurrent" conformational change were not found from the simulations. On the other hand, the PMF studies have discovered an alternative disentanglement and exchange process which finally leads to the helix-inversion of BBDD. The energy barrier of the helix-inversion of the [**H**, **P**] conformations following the disentanglement and exchange is lower than that of the [**H**, **H**] conformations with no exchange. Therefore, it

is concluded that the inversion of the whole structure takes place with the following process: 1) the disentanglement and exchange of TMS groups at one end of BBDD, followed by 2) the helix-inversion, and finally 3) the disentanglement and exchange of TMS groups at the other end. In addition, the study suggests that the disentanglement and exchange process could potentially be the rate-determining process to helix-inversion. It is noted that these processes occur on timescales shorter than nanoseconds and would be difficult to detect directly in experiments. The overall process might still appear to experimental NMR studies as “concurrent”. The results found in this section provided new insights as to how one could potentially design new functional double-helical molecules by making use of disentanglement and exchange process for helix-inversion in practical applications.

3. Stacked Structures of a Double-stage COF

3.1. Introduction

The previous section described the importance of local structures and dynamics of the terminal TMS groups on the function of helix-inversion. Not only the local structures and dynamics but also global structures can affect functions of materials, represented by porous materials, which could be applicable in diverse areas such as gas storage and catalysis utilizing the global structures with many nanosized pores.[68,69] One class of such attractive crystalline porous materials are porous coordination polymers (PCPs) / metal organic frameworks (MOFs) having advantages in designability of framework structures and tunability of pore size to express various functions.[69] COFs, another class of porous crystalline materials emerged in 2005, are often 2D organic co-polymers in which at least two different classes of monomer units are connected via covalent bonds to form large surface sheets which can be stacked on top of each other via π-π interactions.[29] The columns then form 1D pores whose sizes could be determined by the choice of the monomer units. COFs exhibit low densities and higher thermal stabilities than organic molecules.[30,31,70] They have been shown to express various functions, which are affected not only by the local structures of the monomer units, but also by the global structure of the framework.[29,63,71-77] Unfortunately, structural characterization of COFs has troubles due to the general difficulties in producing single crystals large enough, which is related to their bond formation processes that show lower reversibility compared with other, more crystalline porous materials such as PCPs/MOFs where coordination bonds are formed in equilibrium reactions in usual.[31-34,78] Rietveld analysis is usually used for COFs to reveal their structures from powder X-ray diffraction (XRD) patterns.[79,80] Construction of initial

model structures is essential in the procedures analyzing these patterns, and the difficulty of such construction is also well known.[81] On the other hand, theoretical prediction of feasible structures has become a practical approach because quantum chemical methods such as DFT can be applied to explore various candidate structures. Thus, theoretical calculations can predict their relative energies and sometimes also the local dynamics of the frameworks, which may also affect the three-dimensional (3D) structures and functions.[35] For such careful investigations it is advisable to use computationally more efficient, approximate DFT methods such as DFTB.

In this section, the geometries, energetics and dynamic properties of various stacking orders of a particular double-stage COF recently synthesized by Jiang *et al*. were theoretically investigated.[82] It is constructed from zinc 5, 10, 15, 20-tetrakis(4′-tetraphenylamino) porphyrin (ZnP), 2, 3, 9, 10, 16, 17, 23, 24-octahydroxyphthalocyaninato copper (II) (CuPc) and 4-formylphenylboronic acid (FPBA) under solvothermal conditions. In this condition, boronic ester is formed between CuPc and FPBA, and imine is formed between ZnP and FPBA to build the rectangular COF as shown in Figure 3.1. This COF is called CuPc-FPBA-ZnP. This system was selected because it exhibits a wide variety of monolayer structures due to it being a system consisting of three components, and has formally freely rotatable *p*-phenylene groups that can disturb the stacking order as explained below. Two representative isomers of the CuPc-FPBA-ZnP monolayer were considered, one is square (**S**), having tetragonal pores, while the other is rhombic (**R**), having rhombic pores. In the **S** isomer, the four N atoms of imine around the ZnP units are connected to the *p*-phenylene groups of FPBA forming identical dihedral angles, whereas in the **R** isomer these dihedral angles alternate by 180° for N atoms connected to nearest-neighbored FPBA units. The layer stabilization energies

in various stacking orders of **S** and **R** monolayers were calculated, and theoretically predicted XRD patterns were compared with the experimentally measured one for this COF. To gain deeper insight into the dynamic properties of the *p*-phenylene groups connected to the imine N atoms, the influence of their rotation in one of the optimized 3D structures was investigated.

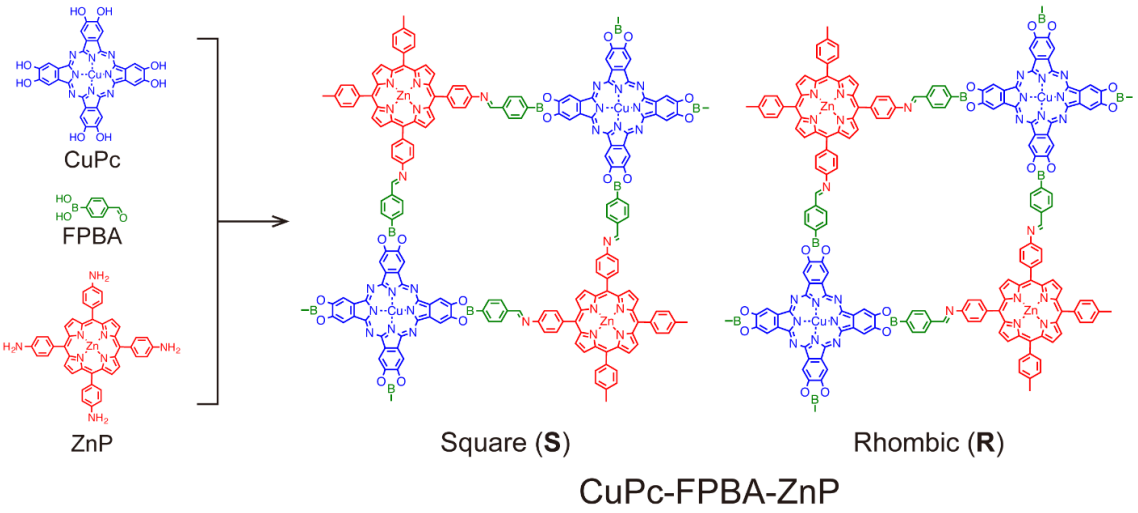

Figure 3.1. Schematic structures of monomers, ZnP (red), CuPc (blue) and FPBA (green), and **S** and **R** isomers of a CuPc-FPBA-ZnP monolayer.

3.2. Computational Details

3.2.1. Quantum chemical calculations

The geometry optimization of the monolayers and their layered structures were performed using the SCC-DFTB method as implemented in the DFTB+ program package version 1.2.2.[19] Lennard-Jones type dispersion with the universal force field (UFF) parameters was included in all calculations to include π-π stacking interactions.[64] The mio Slater-Koster parameters were applied for X and Y (X, Y = C, H, O, and N) element pairs, rscc-materials parameters were applied for B and X (X = B, C, O, and N) element pairs,

borg parameters were applied for B and H element pair, znorg parameters were applied for Zn and X (X = C, H, O, N, and Zn) element pairs, and slko.5425 parameters were applied for Cu and X (X = C, H, O, N, and Cu) element pairs.[19,35,83-85] The parameters of Zn and C, Cu and C, and Zn and C element pairs were used instead of the Zn and B, Cu and B, and Zn and Cu element pairs respectively, because their interactions between each pair in the COF are negligibly small due to the long enough distance between the atoms of each pair. An electronic temperature of 300 K was employed for the total Mermin free energy to accelerate SCC convergence. From now in this section SCC-DFTB including UFF dispersion was referred to as "DFTB" for brevity. Single point DFT calculations of periodic structures with the Perdew-Burke-Ernzerhof (PBE) exchange-correlation functionals with ultrasoft pseudopotentials and the second version of Grimme's dispersion correction (PBE-D2) were performed using the Vienna Ab-initio Simulation Package (VASP) 5.2 to validate the computed DFTB energies. 400 eV for energy cutoff and 1×10^{-6} a.u. for the total free energy and band structure energy change were employed as each threshold for DFT calculations of periodic systems.[86-91]

To obtain the rotational barriers of *p*-phenylene groups with DFTB, relaxed scan calculations of isolated systems were performed using Gaussian 03.E.1 based on the forces calculated by DFTB+.[92] DFT single point calculations of the isolated monolayer structures obtained from the relaxed scan by SCC-DFTB were performed using Gaussian 09.D.1.[93] The PBE exchange-correlation functional and 6-31G(d,p) basis set was used for C, H and N atoms and LanL2DZ was used for Zn atoms. To include dispersion interaction, the DFT-D2 method is adopted for the consistency with the periodic calculations.[15,94]

The optimization of atomic geometries and all three lattice vectors were performed in periodic boundary conditions (PBC) using the γ-point approximation. The conjugate

gradient algorithm was employed in geometry optimizations using 1×10^{-3} Ha/a_0 as a force threshold. 100 Å and 4.5 Å were used as initial distances separating adjacent 2D monolayers in the optimizations of individual monolayer geometries and stacked structures, respectively.

3.2.2. Design of monolayer models

Unit cells of **S** and **R** isomers are shown in Figure 3.2. Each isomer can have four distinct rotational conformers distinguished by the orientations of *p*-phenylene groups around ZnP, which should twist out of the plane due to steric hindrance between their *ortho*-hydrogen and the closest hydrogen atoms of the ZnP unit (see Figure 3.3). these local conformers were named C_2, C_4, S_4, and C_2xy, based on their local symmetries. The geometries of these eight monolayer structures were optimized and labeled individually, for instance the **S** isomer with C_2 conformation was named **S**_C_2.

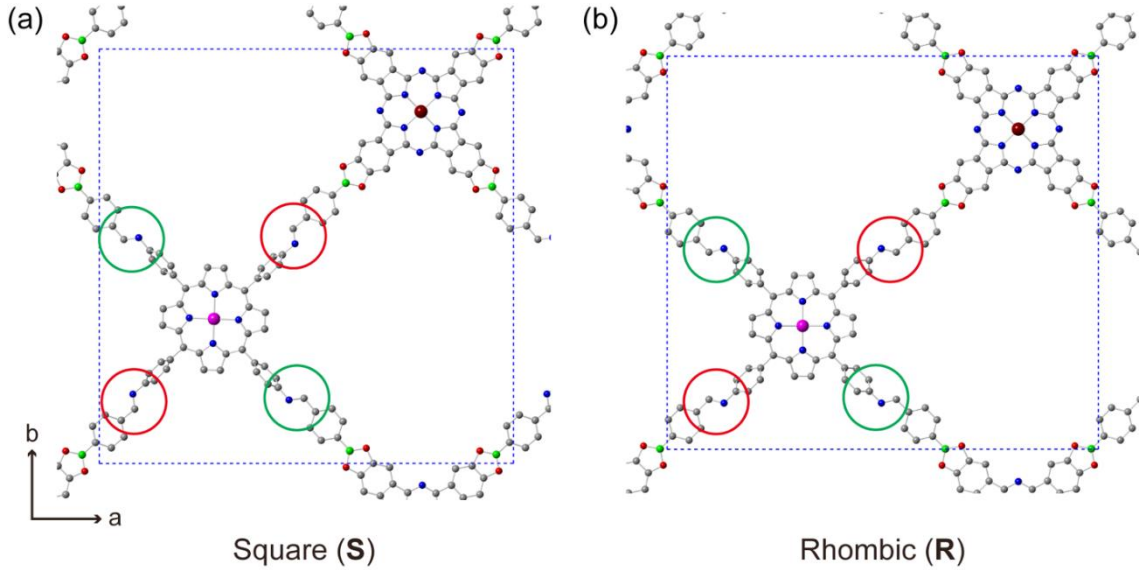

Figure 3.2. The geometries of the COFs in each unit cell of (a) **S** and (b) **R** forms. The gray, blue, red, green, magenta, and brown spheres indicate C, N, O, B, Zn, and Cu, respectively. H atoms are omitted for clarity. Blue dashed lines indicate the unit cells. Imine bonds in the red circles are reverse while those in the green circles are same.

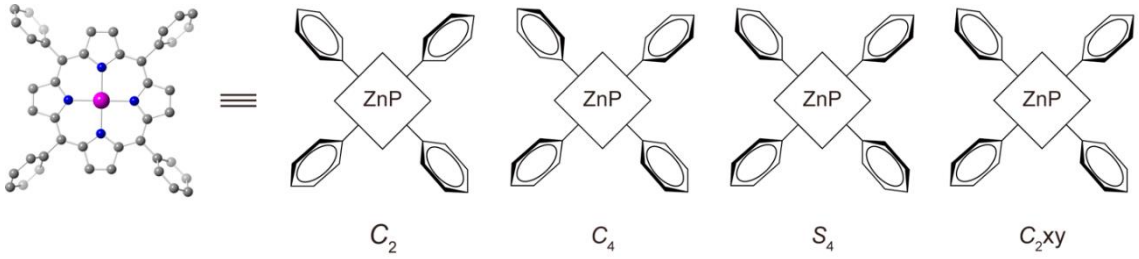

Figure 3.3. Rotational patterns of the four phenyl rings of the FPBA unit connected to a ZnP unit. The gray, blue, and magenta spheres are C, N, and Zn, respectively. H atoms are omitted for clarity.

3.2.3. Design and characterization of stacked structure models

Within one unit cell two layers of the optimized monolayer were stacked for each C_2, C_4, S_4, and C_2xy conformers of each **R** and **S** forms as initial structures as shown in Figure 3.4. For the **R** isomer, eight different types of vertical stacking order were considered, namely eclipsed (**E**), staggered (**SG**), serrated x directon (**SR-x**), serrated y direction (**SR-y**), serrated xy direction (**SR-xy**), inclined x direction (**I-x**), inclined y direction (**I-y**), and inclined xy direction (**I-xy**) types. The importance of the stacking order in COFs is well illustrated in a previous study.[67] **E** shows perfectly eclipsed vertical stacking. **SG** is a staggered structure in which a vertex of one layer is positioned below the center of the pore of the next layer. **SR-x**, **SR-y** and **SR-xy** are repetitive structures in which the second layer slips slightly in the x, y and xy directions from **E**, respectively, and the third layer (which is in the periodic copy of the unit cell) is perfectly eclipsed with the first layer. Thus, the unit cell angles α and β, measuring the direction of the unit cell vector involved in vertical stacking, are 90° in these structures. **I-x**, **I-y** and **I-xy** are slipped structures in x, y and xy directions, respectively, but here the third layer is also slipped by the same angle against the second layer as the second layer is against the first. Hence, in inclined **I**

structures, $\alpha, \beta < 90°$. In the case of the **S** isomer, **SR-y** and **I-y** can be omitted because x and y directions are equivalent. The initial slipping distance in **SR** and **I** is 1.0, 1.5 and 2.0 Å for the **S** form and 1.5 Å for the **R** form, as discussed later. Thus, 56 different stacked structures were considered for the **S** isomers and 32 different stacked structures were considered for the **R** isomers in total as initial structures for the geometry optimization. Two layers were put in one unit cell for all the layered structures to investigate their stacking order. The powder XRD patterns of each optimized structure were simulated using the Mercury 3.3.1 code, using $\lambda = 1.54$ Å.[99-102]

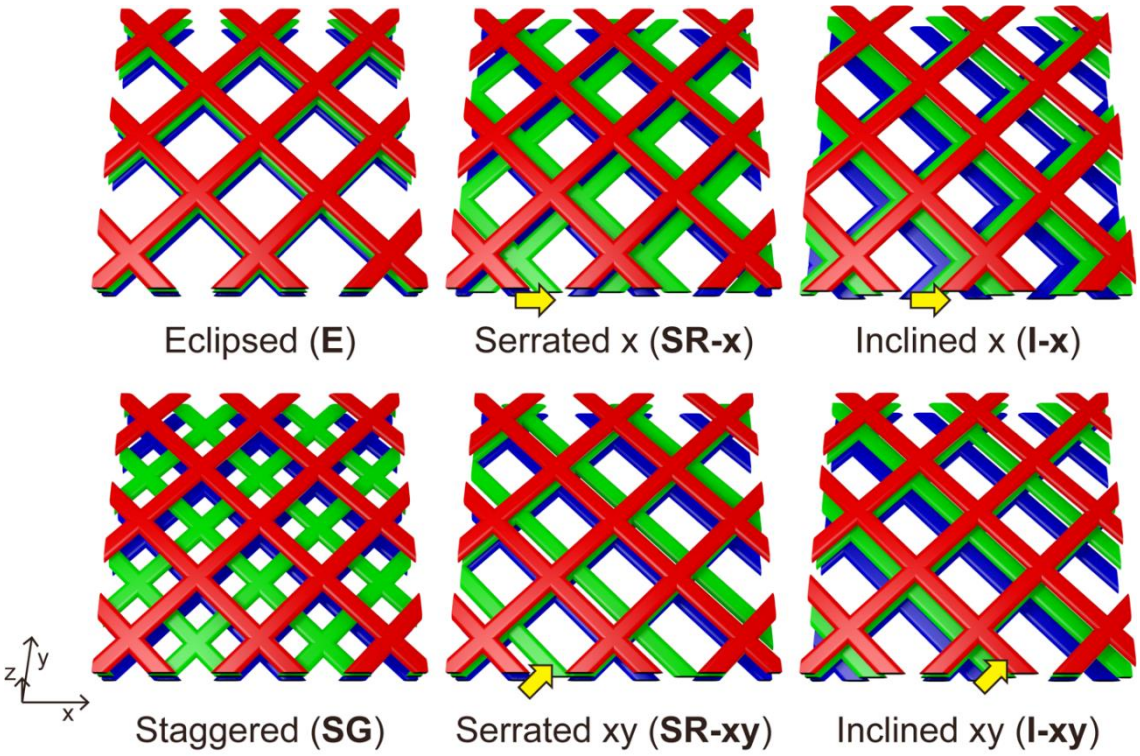

Figure 3.4. Schematic stacking order of the monolayers: Eclipsed (**E**), staggered (**SG**), serrated x (**SR-x**), serrated xy (**SR-xy**), inclined x (**I-x**), and inclined xy (**I-xy**). **SR-y** and **I-y** are omitted because of their similarity to **SR-x** and **I-x**, respectively. Yellow arrows indicate the slipping directions. Three layers were illustrated to show how to stack clearly, although only explicitly two monolayers were included in a single unit cell.

The stacking energy, E_{stack} per unit cell per layer was calculated as follows:

$$E_{stack} = -(E_{layer} / 2 - E_{mono}), \quad (1)$$

where E_{mono} and E_{layer} are the total Mermin free energies of the optimized monolayer structure and the optimized two layers in the unit cells in each stacking types, respectively. E_{layer} should be divided by two because one unit cell contains two explicit layers.

3.2.4. Rotation of FPBA p*-phenylene rings in monolayer and stacked models*

Rotational barriers of the FPBA *p*-phenylene groups surrounding the ZnP units were calculated to elucidate the effect of this rotation on the energetics of particular stacking orders. Since these calculations require higher computational costs, H-terminated molecular models of the COF were constructed. To investigate the size dependency of the molecular model, one small model and one large model were used as shown in Figure 3.5 (b, c). The rotational barrier was estimated by performing relaxed scans of the isolated monolayer models by changing the dihedral angle, θ, between the rotating *p*-phenylene group and the porphyrin ring as shown in Figure 3.5. Single point calculations using PBE-D2 of the optimized structures by DFTB at each angle were also carried out to compare the rotational barriers between DFTB and DFT results. Following the evaluation of rotation of *p*-phenylene groups in the monolayer model calculations, the influence of neighbor layers on the rotational barrier in the molecular models was investigated. A three-layered model and fixed terminal C and N atoms were used as shown in Figure 3.5 during optimization to reproduce the rigid crystal environment, for each of small and large models.

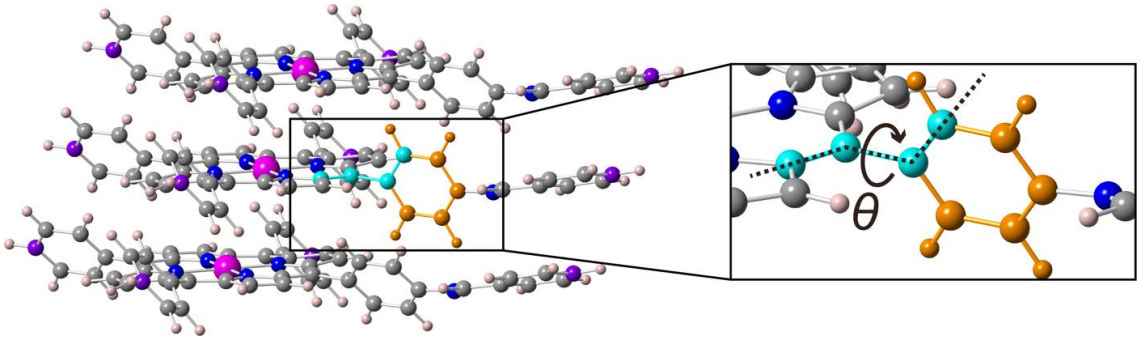

Figure 3.5. Side view of smaller 3-layered model of **1**. The phenyl group with orange color is rotated from θ = 0° to 360°. Coordinates of terminal carbon atoms with purple colors are fixed during optimization. The gray, blue, pink and magenta spheres are C, N, H and Zn, respectively.

3.3. Results and Discussions

3.3.1. Structural and energetic evaluation of monolayer structures

The relative energies calculated with DFTB and DFT of each form optimized by DFTB and the Boltzmann distributions at 393 K (120°C, corresponding to experimental synthesis conditions) are summarized in Table 3.1. The structures of **S**_S_4 are the least stable with both DFTB and DFT, while the structures of **R**_S_4 and **S**_C_4 are the most stable with DFTB and DFT methods, respectively. However, both methods distribute the relative energies within a narrow window of only 3 kcal/mol, which is less than 2% of the stacking energy. The inherent accuracy of DFT is less than 3 kcal/mol and therefore it is difficult to draw quantitative conclusions from first principles calculations. However, the Boltzmann distribution is sensitive to such small energy differences and shows that some structures compete in abundance ratios with the most stable structure in each method. These results propose the possibility that under experimental conditions various monolayer isomer structures can be formed, causing different local stacking orders during

the self-assembly process of the 3D global structure. This may also be the reason why preparing single crystals of COFs with sufficiently large size to obtain X-ray crystal structures is difficult.

Table 3.1. DFTB relative energies of monolayer structures of CuPc-FPBA-ZnP after geometry optimization in kcal/mol. Boltzmann distributions at 393 K are shown in parentheses.

Method	**S**_C_2	**S**_C_4	**S**_S_4	**S**_C_2xy	**R**_C_2	**R**_C_4	**R**_S_4	**R**_C_2xy
DFTB	1.73	0.89	2.20	1.53	0.96	1.35	0.00	0.64
	(4%)	(14%)	(2%)	(6%)	(11%)	(7%)	(38%)	(17%)
DFT	1.07	0.00	2.94	1.46	0.27	0.78	1.56	1.97
	(9%)	(37%)	(1%)	(6%)	(26%)	(14%)	(5%)	(3%)

Table 3.2. The initial and optimized layered structures of the **S** isomer and their E_{stack} in kcal/mol. The slipping distances are shown in parentheses in the leftmost column. The optimized symmetrical conformations are shown in parentheses, when optimized ones are different from the initial ones.

Symmetry	C_2		C_4		S_4		C_2xy	
Initial	E_{stack}	Optimized	E_{stack}	Optimized	E_{stack}	Optimized	E_{stack}	Optimized
E	127.3	**E** (**3'**)	104.2	**E**	130.1	**E**	123.0	**I-xy**
SG	68.0	**SG**	66.6	**SG**	70.4	**SG**	68.2	**SG**
SR-x (1.0 Å)	129.1	**E**[a]	105.6	**SR-x**	132.1	**E** (**2**)	127.0	**I-x**
SR-x (1.5 Å)	129.6	**E**[a]	104.9	**SR-x**	131.6	**E**	128.4	**I-xy**
SR-x (2.0 Å)	130.7	**E**[a] (**3**)	105.4	**SR-x**	118.2	**SR-xy** (C_2xy)	109.2	**SR-xy** (C_2xy/C_4)[b]
SR-xy (1.0 Å)	130.0	**E**[a]	106.0	**E**	131.0	**E**	121.5	**SR-xy**
SR-xy (1.5 Å)	130.0	**SR-x**[a]	118.0	**SR-xy** (C_2xy)	117.2	**SR-xy** (C_2xy)	130.0	**SR-y** (C_4/S_4)[b, c]
SR-xy (2.0 Å)	131.5	**SR-xy**	116.0	**SR-xy** (C_4/S_4)[b]	116.3	**SR-xy** (C_4/S_4)[b]	129.5	**SR-y** (C_4/S_4)[b, c]
I-x (1.0 Å)	138.3	**I-x**	113.4	**I-x**	135.7	**I-x**	130.9	**I-x**
I-x (1.5 Å)	139.4	**I-x**	114.8	**I-x**	137.2	**I-x**	132.5	**I-x**
I-x (2.0 Å)	139.5	**I-x**	115.0	**I-x**	132.1	**I-x** (C_2xy)	131.9	**I-x**
I-xy (1.0 Å)	137.9	**I-xy**	114.5	**I-xy**	138.4	**I-xy**	134.0	**I-xy**
I-xy (1.5 Å)	139.5	**I-xy**	133.9	**I-xy** (C_2xy)	134.9	**I-xy** (C_2xy)	134.4	**I-xy**
I-xy (2.0 Å)	140.1	**I-xy** (**1**)	133.8	**I-xy** (C_2xy)	135.1	**I-xy** (C_2xy)	134.3	**I-xy**

[a]Zn and N atoms in ZnP form bonds between adjacent layers. [b]The each layer in one-unit cell has different symmetry. [c]The structure inclined in y and –x directions and serrated in y direction.

Table 3.3. The initial and optimized layered structures of the **R** isomers and their E_{stack} in kcal/mol. The optimized symmetrical conformations are shown in parentheses, when optimized ones are different from the initial ones.

Symmetry	C_2		C_4		S_4		C_2xy	
Initial	E_{stack}	Optimized	E_{stack}	Optimized	E_{stack}	Optimized	E_{stack}	Optimized
E	126.2	**I-x**	105.2	**E**	127.6	**E**	125.3	**I-(x-y)**[b]
SG	66.9	**SG**	66.6	**SG**	67.6	**SG**	67.0	**SG**
SR-x	128.9	**SR-x**[a]	104.8	**SR-x**	129.3	**E**	123.2	**SR-x**
SR-y	130.0	**E**[a]	103.4	**SR-y**	129.5	**E**	121.1	**I-(y-x)**[c]
SR-xy	130.7	**E**[a]	117.9	**SR-xy** (C_2xy)[b]	128.9	**E**	121.9	**SR-xy**
I-x	136.1	**I-x**	114.6	**I-x**	131.8	**I-x**	131.2	**I-x**
I-y	135.4	**I-xy**	114.6	**I-y**	133.9	**I-y**	127.7	**I-y**
I-xy	138.0	**I-xy**	115.6	**I-xy**	136.1	**I-xy**	129.9	**I-xy**

[a]Zn and N atoms in ZnP form bonds between adjacent layers. [b]The structure slipped in +x and –y directions. [c]The structure slipped in +y and –x directions.

3.3.2. Structural and energetic evaluation of stacked structures

A variety of structures of the COF were obtained from not only the diversity of local stuructures such as the rotational conformations of the *p*-phenylene groups explained above but also global structures such as layered manner of the each monolayer. Different COF structures can be provided by considering different local rotational conformations of the *p*-phenylene groups within each monolayer, in addition to the stacking arrangement of individual monolayers. The list of all optimized stacked 3D structures of the **S** isomers and their E_{stack} are shown in Table 3.2.

We first focus on the dependency of the initial slipping distances on the optimized structures. We optimized the structures of **I** and **SR** stacking orders with initial slipping distances of 1.0, 1.5 and 2.0 Å. While inclined **I** structures remained inclined during geometry optimization regardless of the different initial slipping distance, some of the serrated **SR** structures changed stacking order during geometry optimizations. For instance, **SR** type structures with an initial slipping distance of 1.0 Å tend to change to **E** type structures during optimization, while optimization with an initial distance of 2.0 Å tends to maintain **SR** type. For an initial distance of 1.5 Å, the optimized structure becomes either **E** or **SR** types. We adopted the initial distance of 1.5 Å for the optimization of the **R** isomers, as an analogous case of the **S** isomers. The list of the optimized stacked structures of the **R** isomers and their E_{stack} are shown in Table 3.3. The most stable structure, **S**_C_2-**I-xy** showed the largest E_{stack}, 140.1 kcal/mol among those we optimized in this thesis. This overall most stable structure was chosen among all optimized 3D structures and labeled **1** for simplicity. In order to understand the origin of its stability, the stacking energies of each isolated COF component were calculated using

molecular, hydrogen-terminated models (i.e. CuPc-BA, FP1-4, ZnP_ring, Ph1-4, CuPc-FPBA, ZnP-Ph) shown in Figure 3.6 to clarify the contributions from each component. The stacking energy of each component, E_{s_cmpt}, was defined as follows:

$$E_{s\_cmpt} = -(E_{dimer} - E_{mono1} - E_{mono2}), \quad (2)$$

where E_{dimer} is the single-point energy of the 2-layer model of each component and E_{mono1} and E_{mono2} are the single-point energies of each single component, respectively, evaluated at the geometries obtained from the optimized crystal structure.

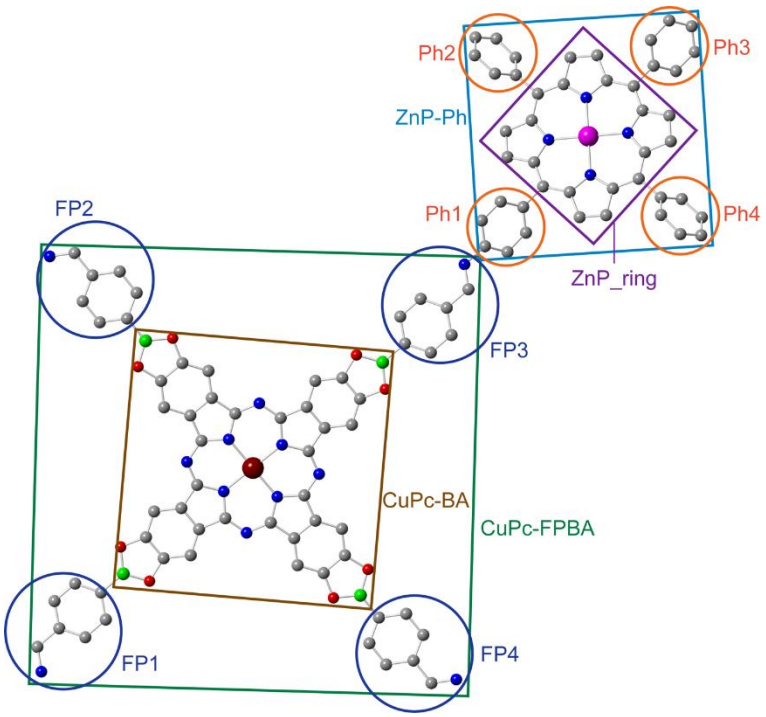

Figure 3.6. Definition of the components for the calculation of E_{s_cmpt}. The each component of CuPc-BA (brown square), ZnP_ring (purple square), FP1-4 (dark blue circles) Ph1-4 (orange circles), CuPc-FPBA (green square) and ZnP-Ph (cyan square) are shown. Each model was terminated by hydrogen atoms. The gray, blue, red, green, magenta, and brown spheres indicate C, N, O, B, Zn, and Cu, respectively. H atoms are omitted for clarity.

Each pair of the components in the adjacent layers stacked within the distance of 3.2 to 3.6 Å. E_{s_cmpt} of each component of **1** is listed in Table 3.4. Larger components represented by CuPc-BA tend to show larger stabilization. These stacking stabilizations made **1** the most stable structure with largest E_{stack}, although the monolayer of **1** was less stable than the optimized **S**_C_2 monolayer by 12.1 kcal/mol. The mean rotational dihedral angle of the four *p*-phenylene groups around ZnP in **1** is 50.6°, which is smaller than that in the **S**_C_2 monolayer, 70.1°. As shown in Table 3.5, **1** has the cell parameters of $\alpha < 90°$ and $\beta < 90°$ because of the inclination of the structure in xy direction, which means that **1** is not perfectly rectangular but actually belongs to the triclinic crystal systems. Figure 3.7(a) shows the simulated XRD pattern of **1**, which has the largest peak around $2\theta = 3.6 \sim 3.7°$, assigned to $(1\ \bar{1}\ 0)$, at a similar position to the experimental one. However, the simulated XRD of **1** does not match experiment due to the additional peak around $2\theta = 4.0°$, assigned to (110). We found that some structures of the **R** isomers showed E_{stack} close to that of **1**. For instance, the most stable structure of the **R**isomers, **R**_C_2-**I-xy**, showed a slightly smaller E_{stack} than **1** (138.0 kcal/mol), and the XRD pattern of it was also inconsistent with experiment, as shown in Figure 3.8. Afterwards, the XRD patterns of all optimized stacked 3D structures were selected, and then the structures having only one peak consistent with experimental XRD data were selected. The structure with the largest E_{stack} among them is **S**_S_4-**E** (named **2**) with an E_{stack} of 132.1 kcal/mol, which is 8.1 kcal/mol smaller than **1**. The E_{s_cmpt} of each component in **2** is listed in Table 3.4. Compared to **1**, the small components of **2** have similar or larger E_{s_cmpt}, while the combined components of **2** have smaller E_{s_cmpt}. We assumed that the stabilizations of each component with lateral components in **1** are larger than those in **2**. The mean rotational dihedral angle of the *p*-phenylene groups around ZnP in **2** is 41.5°, which is

smaller than that observed in **1**. The simulated XRD pattern of **2**, shown in Figure 3.7(b), agrees with experiment. As shown in Table 3.5, **2** has the cell parameters of α = 90.0°, β = 90.2°, γ = 90.0° and $a = b$ = 34.4 Å, which imply that **2** could be categorized as a tetragonal crystal system. In the tetragonal crystal system, the planes (110) and $(1\ \overline{1}\ 0)$ are equivalent. As summarized in Table S3.1 and Table S3.2, the **I** type structures, including **1**, tend to show higher stability and larger E_{stack}, although they disagree with the experimental XRD pattern. It is suggested that inclination between monolayers reduces the steric repulsion between them, especially between the twisted *p*-phenylene groups around ZnP. The conformational relaxation with smaller steric hindrance in the monolayer of **I** results in larger E_{stack} compared to **E**, **SR**, and **SG**. However, the stabilization in **I** is purely enthalpic in nature, because it is obtained from optimized geometries and does not contain thermal (entropic) effects. Under experimental COF synthesis conditions at 120°C, thermal structural fluctuations such as rotations of the *p*-phenylene groups around ZnP are expected to show significant influence on the stacking order, since the monolayers with different phenylene conformations had relative energies in a so small range that various structures can be formed easily.

Table 3.4. E_{s_cmpt} of each component of **1** and **2** in kcal/mol.

Part		**1**	**2**
		E_{s_cmpt}	E_{s_cmpt}
	CuPc-BA	39.0	38.4
	FP1	2.6	6.0
	FP2	5.1	6.0
	FP3	5.7	6.0
Small	FP4	3.1	6.0
components	ZnP	22.7	23.4
	Ph1	3.7	4.0
	Ph2	4.0	4.0
	Ph3	3.7	4.0
	Ph4	4.0	4.0
Combined	CuPc-FPBA	84.6	79.8
components	ZnP-Ph	47.1	45.8

Table 3.5. Cell parameters of **1** and **2**.

Cell parameters	**1**	**2**
a / Å	34.2	34.4
b / Å	34.2	34.4
c / Å	7.9	7.3
α / °	72.7	90.0
β / °	74.2	90.2
γ / °	90.4	90.0

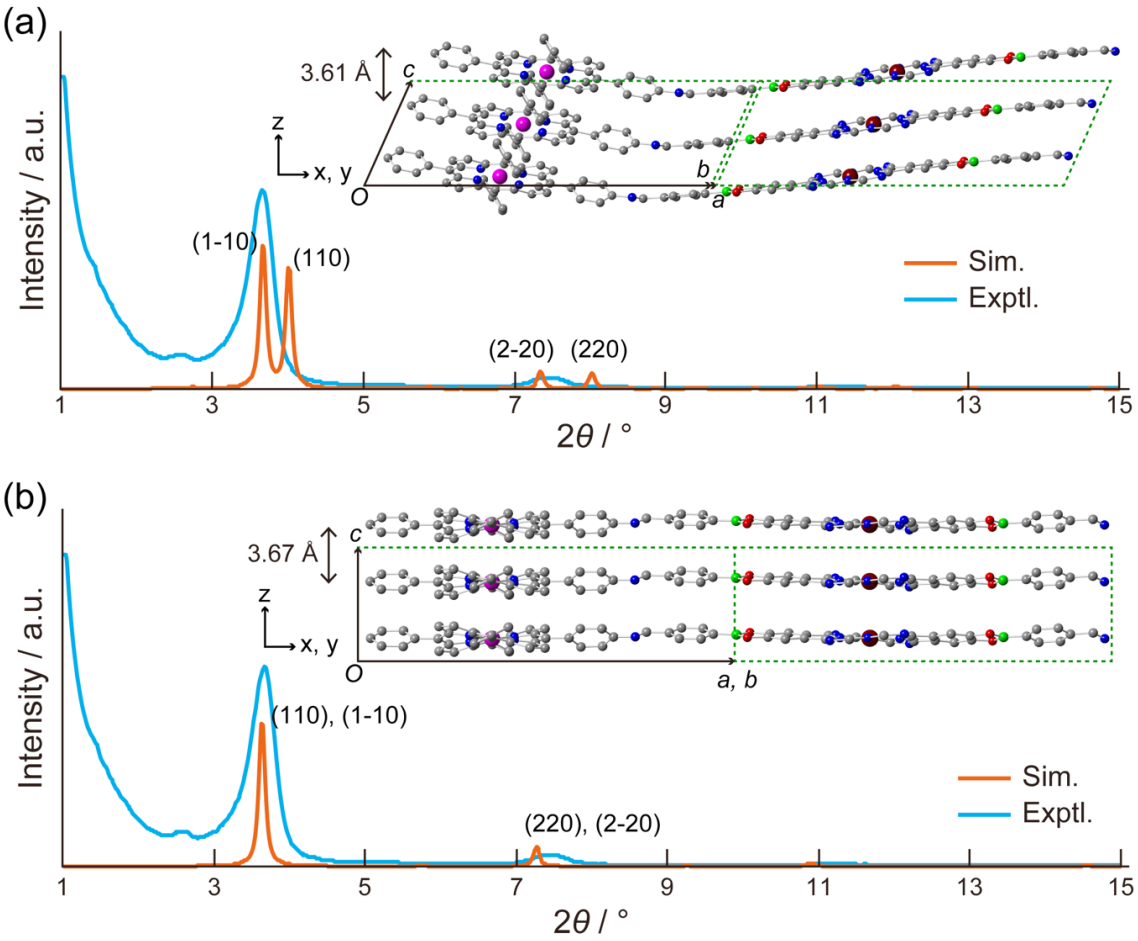

Figure 3.7. (a) The simulated XRD pattern of **1** (orange) and the experimental XRD

pattern (cyan). Side view of **1** is inserted. (b) The simulated XRD pattern of **2** (orange) and the experimental XRD pattern (cyan). Side view of **2** is inserted. Three layers were illustrated to show how to stack clearly, though the two layers model in a unit cell was employed.

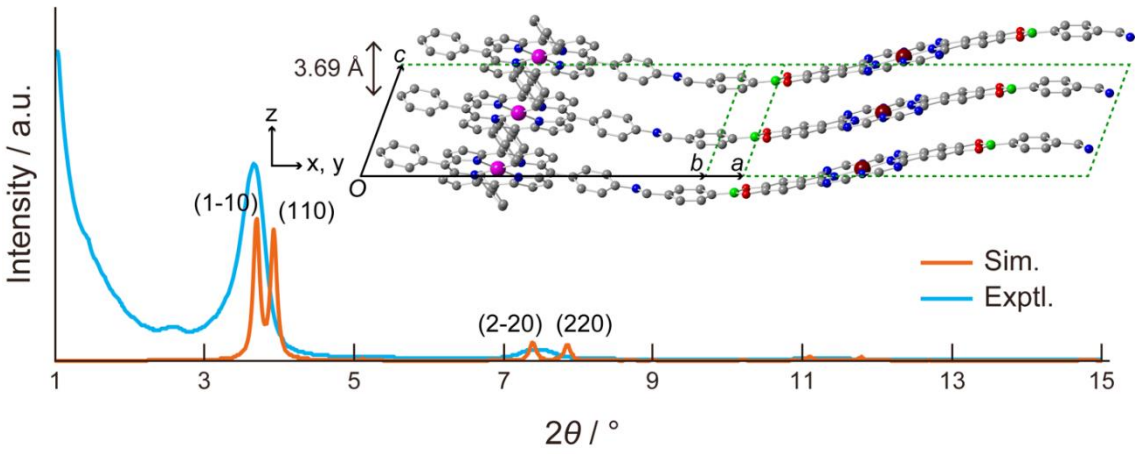

Figure 3.8. The simulated XRD pattern of the most stable **R** form structure (orange) and the experimental XRD pattern (cyan). Side view of the structure is inserted. Three layers were illustrated to show how to stack clearly, though the two-layer model in a unit cell was employed.

3.3.3. Rotation of FPBA p*-phenylene groups*

The discussion regarding the conformation of *p*-phenylene rings around ZnP suggests that their rotation seems to play an important role in the formation of the stacked structures of the COF. The rotational barrier along the dihedral angle θ was calculated to clarify the relationship between the rotational dynamics and the stacking order of the 3D structure. It was defined as $\theta = 0°$ for optimized geometry **1**, which corresponds to a dihedral angle of 49.7° between the planes of the *p*-phenylene ring and the ZnP units. As

shown in Figure 3.9(a), the smaller and larger monolayer models show the energy curves with similar rotational barriers and profiles, indicating that the smaller model is large enough to discuss the rotational barrier in the monolayer case. The rotational barrier of the monolayer model calculated by DFTB, 12 kcal/mol shown in Figure 3.9(a), indicates that complete rotation of the *p*-phenylene groups can occur at room temperature, with wide minima around 45° and 225°, where the rotating *p*-phenylene groups and the porphyrin ring are almost perpendicular. These potential energy wells make large vibration amplitudes feasible. The DFT single point energies calculated at DFTB-optimized geometries, shown in Figure 3.10, make a similar profile to that predicted by DFTB, which validate using it for the calculation of rotational barriers in stacked molecular models.

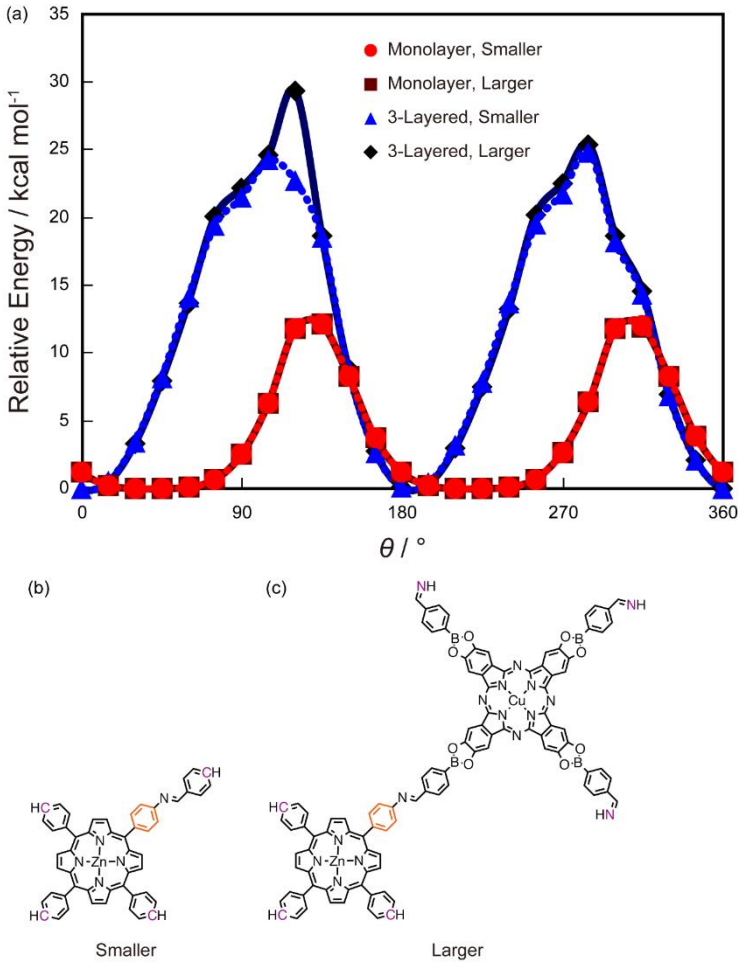

Figure 3.9. (a) Rotational energy barrier of the phenyl group for each model. (b) Schematic model structures of smaller and (c) larger models picked up from **1**. Orange colored phenyl groups indicate the rotating rings. Terminal carbon and nitrogen atoms colored by purple color indicate the fixed atoms in all 3 layers during the relaxation of three layered models.

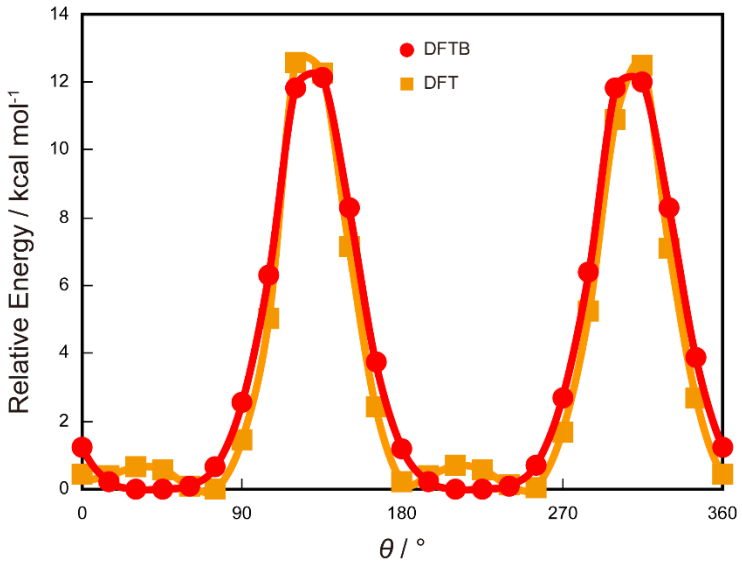

Figure 3.10. Potential energy curve calculated by DFT based on the geometries optimized by SCC-DFTB.

For this purpose, 3-layered isolated models were used and a *p*-phenylene group in the middle layer of each model was rotated as described above. As shown in Figure 3.9(a), the smaller and larger models show the energy curves with similar profiles, except for a disagreement at $\theta = 120°$, which is discussed in the SI. The rotational barrier in the smaller isolated model is 25 kcal/mol, which is larger than that in the monolayer model, and it is certainly not possible to be overcome at room temperature. The minimal energy in the layered model located at $\theta = 0°$. For the layered model the range of rotation of the *p*-phenylene groups was ~ 30° around 0° and 180°, which is much narrower than the range observed in the monolayer model, ~75° around 45° and 225°. These differences are due to the steric repulsion between the rotating *p*-phenylene groups and the adjacent layers, which restricts rotation to a narrower range and increases the rotational barrier in the layered model. The restriction of rotation can prevent forming the thermodynamically most favorable structure, and finally lead to the formation of layered structures with a **SR**

type as a whole, or more complicated stacking order.

3.4. Conclusions

The structural diversity of a double-stage COF, CuPc-FPBA-ZnP was theoretically investigated. Three units of this COF enables to form a large variety of local structures, as well as different stacking orders and rotational vibration of linkers. First, isomeric monolayers of CuPc-FPBA-ZnP were optimized using quantum chemical calculations and showed the competitiveness of various isomers, which indicates difficulty of forming a well-ordered single crystal, as observed in experiment. Second, stacked structures with various stacking orders based on the optimized monolayer structures were optimized. It was found that an inclined **I** type structure, **1**, possesses the lowest potential energy and the largest stacking energy E_{stack}. However, the simulated powder XRD pattern of **1** is inconsistent with the experimental results, while those of some **E** and **SR** type structures reproduced the experiment well. It was suggested that this disagreement arised from the lack of considering thermal structural fluctuation of frameworks in the optimization process of the COF. This is corroborated by the theoretically calculated shallow rotational barriers of the FPBA *p*-phenylene groups around ZnP in the monolayers as opposed to the higher rotational barriers separating steep potential energy wells after stacking. It was concluded that the *p*-phenylene rotation during layer formation produces various isomers. As a result of small differences in the relative energy among the isomers, various other conformational isomers are competitive with the global minimum energy structure and affect the formation processes of COFs. It is therefore concluded that freely rotatable groups such as *p*-phenylene groups should be avoided for production of more highly crystalline COFs.

4. Dynamics of a Proton-conductive 1D CP

4.1. Introduction

The COF described in the section 3 possesses global 3D structures formed via the covalent bonds and π-π stackings. The framework contains metal ions in the center of the phthalocyanine and porphyrin rings, although they might not involve in the formation of the 3D structures directly. In contrast, frameworks whose 3D structures are constructed from metal ions and organic molecules via coordination bonds between them could show dynamics and functions based on the localized charges. In this section, proton conductivity of the CP consisting of metals and organic molecules is discussed.[69]

Increasing energy demand and concern about depletion of fossil fuels have rapidly driven developments of clean energy sources such as proton exchange membrane fuel cells (PEMFCs), which do not emit greenhouse gas such as CO_2 but water only.[5-7,95] As stated in Section 1, electrolytes of fuel cells play an essential role to transport protons from anodes to cathodes, while preventing electrical contact of the electrodes for efficient power generation. High proton conductivity, low electron conductivity and high thermal and chemical stability are required for the electrolytes. Many of currently used electrolytes represented by Nafion possess water-mediated proton conductivity, which has drawbacks such as limited working temperature at < 100 °C, which limits efficiency of proton conduction, and CO poisoning. Anhydrous proton conduction at > 100 °C reduces CO poisoning and promises high efficiency of proton conduction, which is the advantage over water-mediated electrolytes. Some CPs showing either water-mediated proton conduction or anhydrous proton conduction have been developed, and those could be candidates of the electrolytes of PEMFCs.[96-102] One of advantages of CPs is the wide

structural variety of metal ions and linkers, providing high tunability of the structures for higher conductivity and higher stability.[96] In particular, anhydrous proton conduction by a CP itself without introducing guest molecules, or by guest anhydrous ions with charged CP frameworks, might solve the problems of water-mediated proton conduction mentioned above. However, the anhydrous proton conductivities of the CPs (up to 10^{-3} S cm^{-1}) are quite lower than Nafion (0.13 S cm^{-1} at 75 °C) and insufficient for practical use.[96,102-104] Understanding the proton conduction mechanisms in the CPs will enable us to design CPs with higher anhydrous proton conductivities at > 100 °C.

Synthesis of a proton-conductive 1D CP was reported by Horike et al.[35] The CP consists of 1D chains composed of Zn(II) and phosphate linkers and side phosphate ligands with imidazolium counter cations (ImH_2^+), $[Zn(HPO_4)(H_2PO_4)_2](ImH_2)_2$ (**CP1**) illustrated in Figure 4.1. **CP1** is the first example of proton-conductive CP possessing phosphate groups and protonated heterocycles, reaching the proton conductivity of 2.6×10^{-4} S cm^{-1} at 130 °C from around 55 °C nonlinearly. The XRD measurements revealed that all ImH_2^+ were static at -30 °C, while the half of the ImH_2^+ ions disordered and no disorder of the other half were observed at 75 °C, the former and the latter of which were named **D** (disordered) ImH_2^+ and **S** (static) ImH_2^+, respectively. The disorder is expected to be originated from dynamic motion and the reason of the nonlinear increase of proton conductivity, whereas the details of the proton conduction mechanisms and pathways in **CP1** have not been revealed well. Theoretical investigation of the dynamics of ImH_2^+ and phosphate groups provide us with deeper insight into the proton conduction mechanisms and pathways, and the mechanisms of nonlinear increase of proton conductivity around 55 °C.

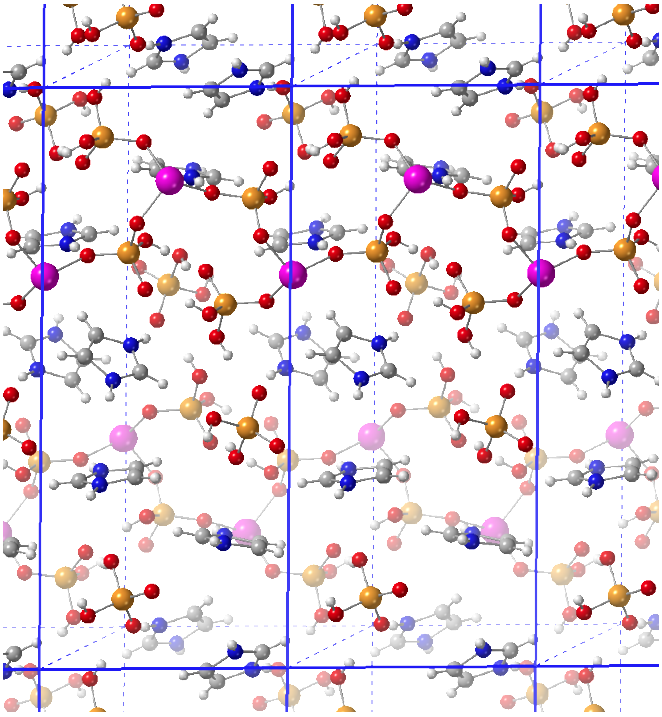

Figure 4.1. Crystal structures of **CP1** at -30 °C. The gray, blue, white, red, orange and magenta spheres are C, N, H, O, P and Zn, respectively. Blue lines show the unit cells.

In this section, static quantum chemical calculations using the DFT method were performed to elucidate the structural properties of **CP1**. The static calculations revealed that the stability of the system depends on the orientation of **D** ImH_2^+, which changes stabilization by the hydrogen bonds between **D** ImH_2^+ and surrounding phosphate groups. MD simulations using the DFTB method were also performed to investigate dynamics of proton conduction of **CP1**. The dynamic calculations suggested that the **D** ImH_2^+ shows stepwise orientation changes rather than free rotation at the timescale of ps. Proton transfer between the phosphate groups was observed while proton transfer involving ImH_2^+ was not observed because the acidity of ImH_2^+ is not enough for proton transfer in **CP1**. These results indicate that the proton conduction occurs via proton transfer reactions between the phosphate groups, and the ImH_2^+ ions are not directly involved in the proton

conduction pathways although they contribute the stabilization of the system by hydrogen bonds with the phosphate groups.

4.2. Computational Methods

Geometry optimization of the crystal structure of **CP1** obtained at -30 °C (**L**) and the two crystal structures at 75 °C (**H1** and **H2**) (Note: the **D** ImH_2^+ disordered at two orientations, and both structures are used to prepare the initial structures for calculation) shown in Figure 4.2 was performed using DFT implemented in the QUANTUM ESPRESSO program package version 6.2.1.[105,106] The projector augmented wave (PAW)-type pseudopotentials with the PBE exchange-correlation functionals obtained from pslibrary were used.[86,107,108] The cutoff of the kinetic energies for the wavefunctions and for the charge density and potential were 60 Ry and 720 Ry, respectively. Periodic boundary conditions with 1×1×1 k-points were applied. The experimental unit cells were during the geometry optimization, named "f-cell" calculations. After the calculations, both atomic positions and unit cells of **CP1** were optimized, named "o-cell" calculations. The names of the experimental structures, i.e. **L**, **H1** and **H2**, were also used as the names of the optimized geometries. To compare the differences of the optimized geometries among **L**, **H1** and **H2** structures, root mean square distances (RMSDs) were calculated between each isolated system of the whole system, 1D chains, **S** ImH_2^+ and **D** ImH_2^+ of both f-cell and o-cell. The C and N atoms of one **D** ImH_2^+ or all **D** ImH_2^+ in the f-cell were exchanged and optimized with DFT, namely pseudo-rotation as shown in Figure 4.3, to clarify the most stable orientation of **D** ImH_2^+. For analysis of orientation of ImH_2^+, the angular parameter, φ, is defined as shown in Figure 4.4.

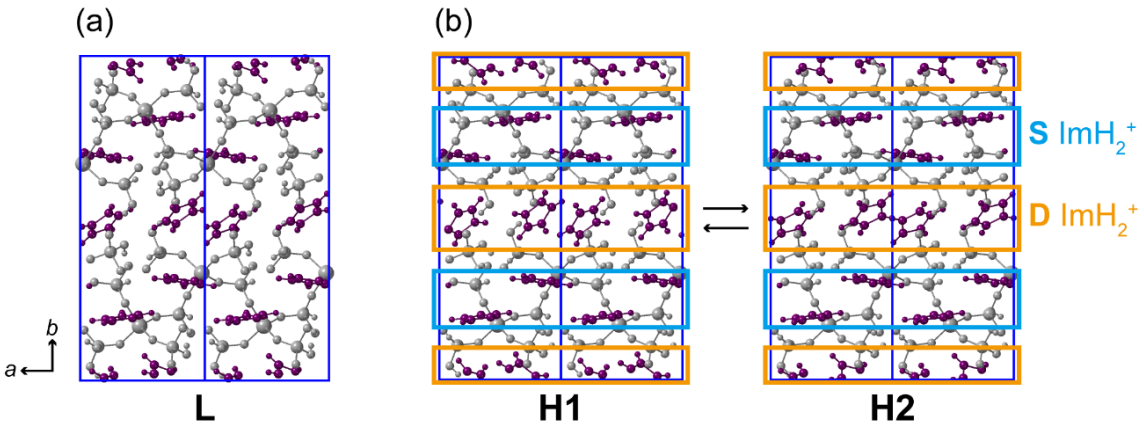

Figure 4.2. Crystal structures of **CP1** at (a) -30 °C and (b) 75 °C. Gray and purple spheres indicate the 1D chains in the framework and ImH_2^+ ions, respectively. Blue lines show the unit cells. ImH_2^+ ions in the light blue and orange rectangles in (b) are **S** ImH_2^+ and **D** ImH_2^+, respectively.

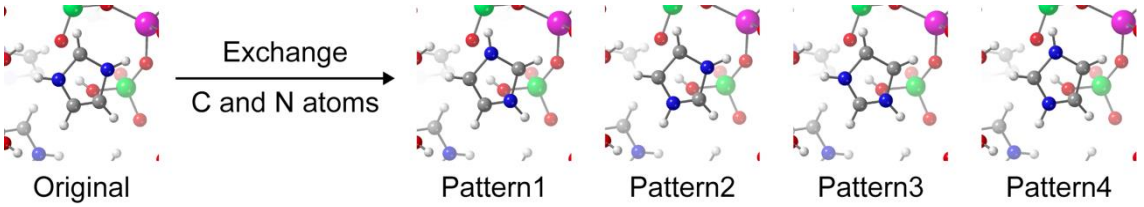

Figure 4.3. Each initial orientation of exchange of C and N atoms (pseudo-rotation) of **D** ImH_2^+. White, gray, blue, red, green and magenta spheres indicate H, C, N, O, P and Zn atoms, respectively.

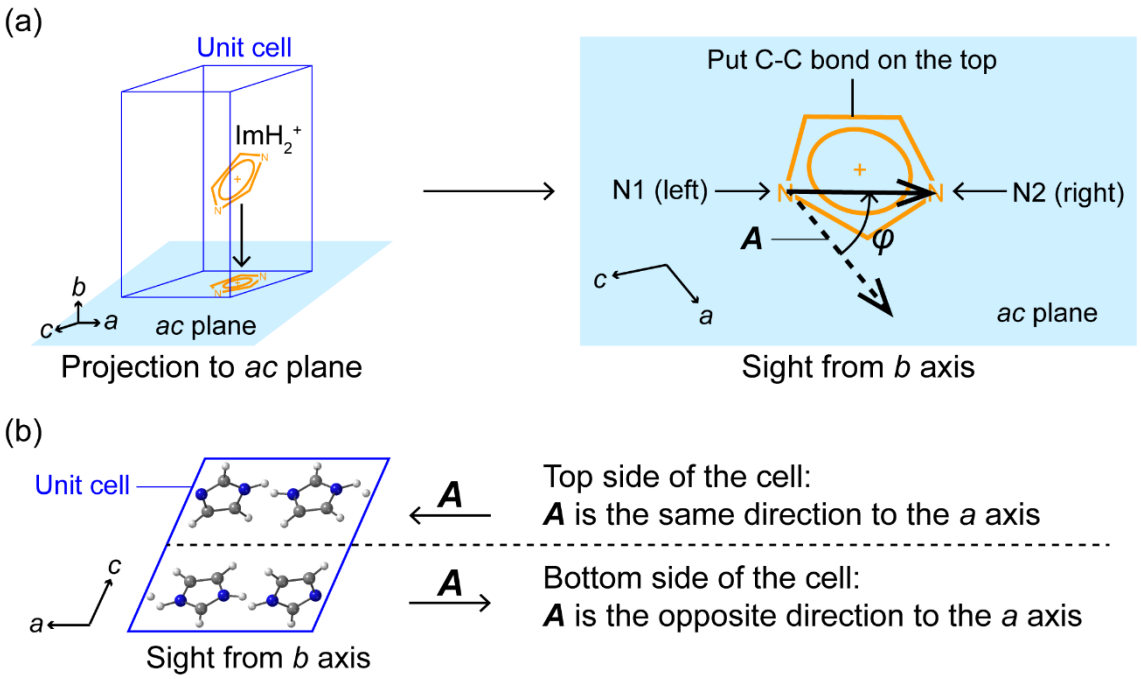

Figure 4.4. (a) Definition of the angular parameter φ. (b) Definition of the direction of ***A***, a vector parallel to the *a* axis used for the definition of φ. White, gray and blue spheres indicate H, C and N atoms, respectively.

The experimental **L**, **H1** and **H2** geometries of **CP1** were optimized using DFTB third order (DFTB3) under f-cell.[20,21] The 3ob-3-1 Slater-Koster parameters were applied.[109-111] Grimme D3 dispersion correction was included.[112,113] In this section, DFTB3 with D3 dispersion correction was abbreviated as DFTB, and MD with DFTB was abbreviated as DFTB-MD. All DFTB calculations were performed on the DFTB+ program package version 17.1 and 18.2.[61] Using the optimized geometries with DFTB as the initial geometries, DFTB-MD simulations for 200 ps were carried out after the equilibrations of 60 ps with the time step of 0.4 fs. Nosé-Hoover NVT ensemble at 243.15 K (-30 °C) and 348.15 K (75 °C) was employed for each initial structure. Each trajectory is named using the name of the experimental structure and the MD temperature, such as "$\mathbf{L}_{\mathbf{243K}}$". To

estimate energy barriers of proton transfer from ImH_2^+ to a phosphate group and between two phosphate groups, single point calculations are performed with DFTB by changing N-H bond distance of ImH_2^+ (d_{NH}) or O-H bond distance of a phosphate group (d_{OH}) of each of the **L**, **H1** and **H2** in f-cell.

4.3. Results and Discussions

The relative energies of the optimized geometries and the experimental and optimized cell parameters are summarized in Tables 4.1 and 4.2, respectively. For both of f-cell and o-cell, **L** showed the lowest energy among the three geometries, but the energy differences between **L** and **H2** are very small for f-cell. The **H1** and **H2** geometries showed small energy differences for both of f-cell and o-cell, and similar optimized cells for o-cell, which indicates that **CP1** could form both orientations of **D** ImH_2^+ such as **H1** and **H2** structures at 75 °C. To investigate the structural differences among **L**, **H1** and **H2**, all atoms and fragments of 1D chains, **S** ImH_2^+ and **D** ImH_2^+ contained in a single unit cell were cropped from each of the optimized geometries, and RMSDs between **L** and **H1**, **L** and **H2**, and **H1** and **H2** for each fragment were calculated as shown in Table 4.3. Much larger RMSDs of **D** ImH_2^+ than those of 1D chains and **S** ImH_2^+ indicate that the differences of the optimized geometries are mainly due to the different orientations of **D** ImH_2^+. The differences of the orientations of **D** ImH_2^+ affect the interactions between the **D** ImH_2^+ and surrounding atoms, which determine the energetic stabilizations of **CP1**. Distinguishing C and N atoms from experimental XRD patterns can be difficult in some cases, which suggests that actual orientations of **D** ImH_2^+ might be different from the experimental results, and further investigation of the orientation of **D** ImH_2^+ and the energies are required.

Table 4.1. Relative energy of optimized **H1**, and **H2** with DFT to **L** in kcal mol^{-1} unit.

	f-cell	o-cell
L	0.0	0.0
H1	+0.4	+8.5
H2	+4.8	+13.6

Table 4.2. Cell parameters of the experimental geometries and optimized geometries with DFT.

Cell	Experimental and f-cell		o-cell		
parameter	**L**	**H1/ H2'**	**L**	**H1**	**H2**
a / Å	9.06	9.01	9.12	8.97	9.15
b / Å	21.53	21.83	22.61	22.61	22.27
c / Å	9.18	9.24	9.26	9.28	9.23
α / °	90.00	90.00	90.00	90.00	90.00
β / °	114.20	114.06	113.83	113.37	113.89
γ / °	90.00	90.00	90.00	90.00	90.00

Table 4.3. RMSDs between all atoms or fragments in the optimized geometries with DFT in Å unit.

Structure	Compared pair	RMSD			
		All atoms	1D chains	**S** ImH_2^+	**D** ImH_2^+
f- cell	**L-H1**	1.41	0.19	0.07	2.77
	L-H2	1.64	0.17	0.06	3.26
	H1-H2	0.49	0.08	0.03	0.95
o-cell	**L-H1**	1.43	0.22	0.18	2.78
	L-H2	1.65	0.20	0.24	3.24
	H1-H2	0.51	0.16	0.10	0.95

To obtain deeper insight into the relationship between the orientations of **D** ImH_2^+ and the energies, pseudo-rotation of one **D** ImH_2^+ or all **D** ImH_2^+ followed by geometry optimization with DFT were performed, and the relative energy against the orientation angle φ of a **D** ImH_2^+, were plotted in Figure 4.5. The energy barrier of the pseudo-rotation of one **D** ImH_2^+ is up to 17 kcal mol^{-1}, indicating that rotation of **D** ImH_2^+ could occur at high temperature. The pseudo-rotation of all **D** ImH_2^+ showed higher energy barrier up to 48 kcal mol^{-1} than that of one **D** ImH_2^+ and quite different energy profiles with different positions and heights of pseudo-rotational barriers from that of one **D** ImH_2^+ for each **L**, **H1** and **H2** system, supposed that coincidental rotations of the **D** ImH_2^+ ions are not feasible and some of **D** ImH_2^+ might be correlated to rotate. Only two patterns of pseudo-rotation have been examined here, which indicates that other patterns of coincidental rotations such as those of two or three **D** ImH_2^+ or those with different angles could occur.

The φ of **D** ImH_2^+ in experimental geometries of **L**, **H1** and **H2** are 269.6°, 6.0° and 31.0°, respectively, which are consistent with the local minima of each corresponding energy curve with theoretical pseudo-rotation of all **D** ImH_2^+.

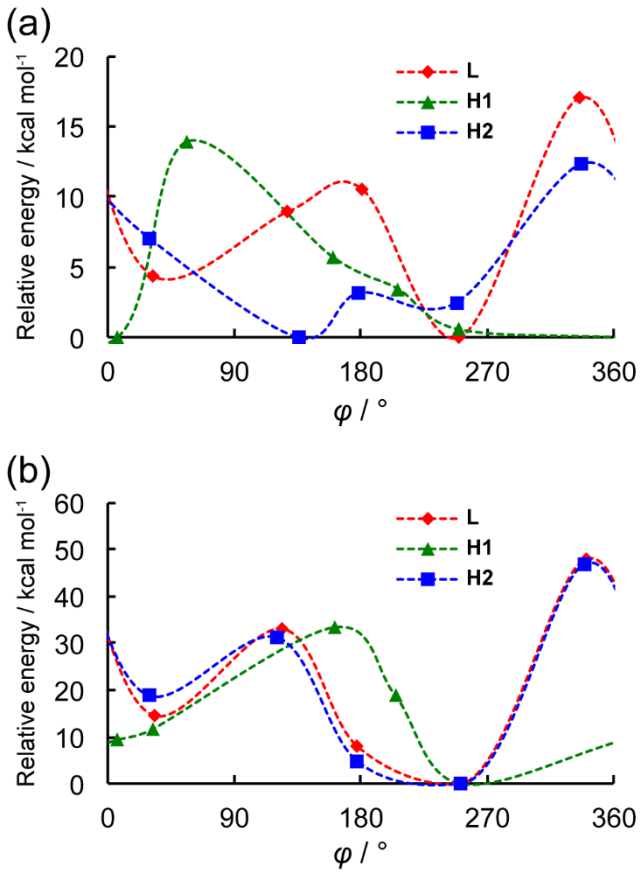

Figure 4.5. Relative energies vs. φ of a **D** ImH_2^+ of the optimized geometries with DFT for (a) pseudo-rotation of one **D** ImH_2^+ and (b) pseudo-rotation of all **D** ImH_2^+. The reference of the relative energies is the most stable optimized geometry for each system.

The geometries around the **D** ImH_2^+ are focused on for investigation of the details of the dependence of the energy on the orientation of **D** ImH_2^+. It was found that the H atoms on the N atoms of ImH_2^+ form hydrogen bonds with O atoms of the surrounding phosphate groups as shown in Figure 4.6, and the hydrogen bond distances depend on the orientation of ImH_2^+. The relative energy and the hydrogen bond distances between the

H and O atoms for each of the pseudo-rotation of one **D** ImH_2^+ and all **D** ImH_2^+ are plotted in Figure 4.7. Because an ImH_2^+ ion can form two hydrogen bonds, we plotted the distance of the shorter hydrogen bond (d_{OH_short}) and that of the longer one (d_{OH_long}) separately. Decreasing hydrogen bond distances of both d_{OH_short} and d_{OH_long} tends to show lower energies of the system, indicating that stronger hydrogen bonds stabilize the system. These results propose that the stability of **CP1** depends on the stabilization by hydrogen bonds depending on the orientation of **D** ImH_2^+.

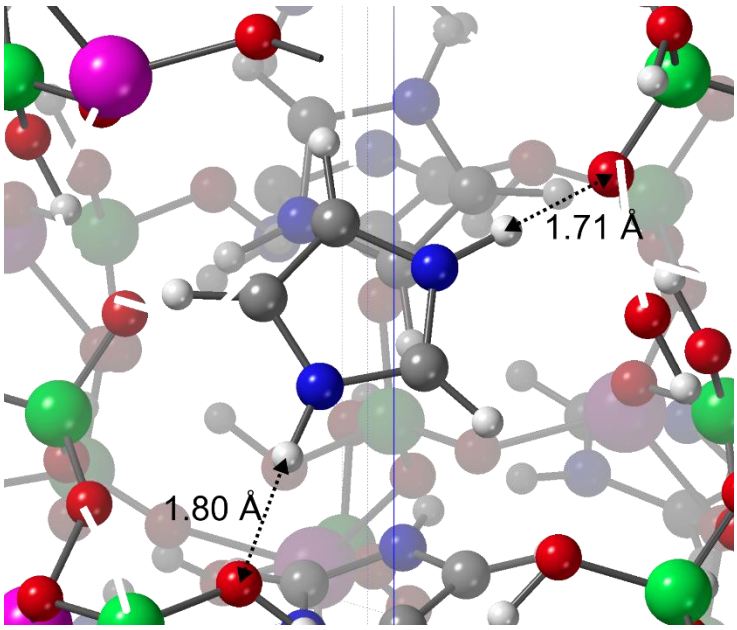

Figure 4.6. Two hydrogen bonds between the H atoms on the N atoms of **D** ImH_2^+ and O atoms of the phosphate groups. White, gray, blue, red, green and magenta spheres indicate H, C, N, O, P and Zn atoms, respectively.

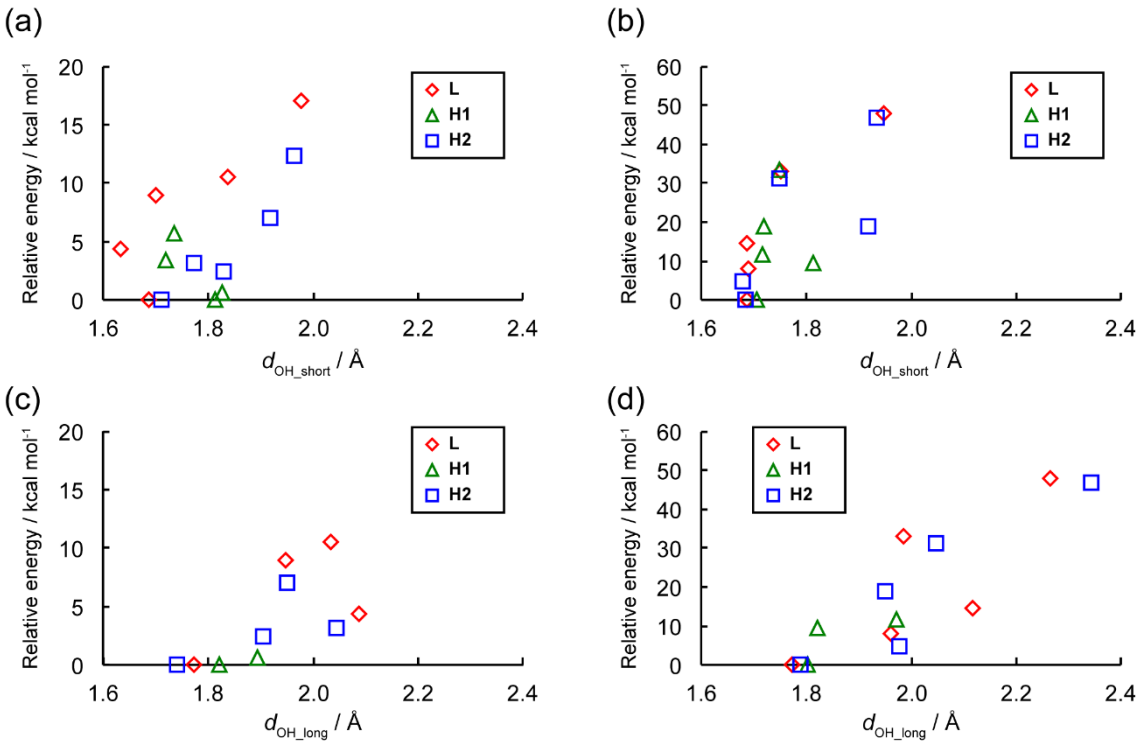

Figure 4.7. Relative energies vs. (a) and (b) shorter O…H hydrogen bond distances d_{OH_short} and (c) and (d) longer O…H hydrogen bond distances d_{OH_long} between the **D** ImH_2^+ and phosphate groups of the optimized geometries with DFT for (a) and (c) pseudo-rotation of one **D** ImH_2^+ and (b) and (d) pseudo-rotation of all **D** ImH_2^+. The reference of the relative energies is the most stable optimized geometry for each system. Only hydrogen bonds shorter than 2.4 Å were plotted.

Detailed rotational dynamics of ImH_2^+ and proton conduction pathways would be obtained from the trajectories of the DFTB-MD simulations. The time courses of the orientation angles φ of four **D** ImH_2^+ are plotted in Figure 4.8. It was found that the **D** ImH_2^+ tends to take two orientations, $\varphi \sim 25°$ and $\varphi \sim 240°$. On the other hand, there are very few distributions between $\varphi = 300°$ and $\varphi = 340°$. To discuss the structural effect on the distributions of φ, three different orientations of **D** ImH_2^+ are shown in Figure 4.9.

Both of the two H atoms on the N atoms of **D** ImH_2^+ forms hydrogen bonds to surrounding O atoms at φ = 238.2° and 26.4° while only one H atom forms hydrogen bonds at φ = 316.8°, which indicates that the distributions of the orientations of **D** ImH_2^+ is affected by stabilization by the hydrogen bonds to the surrounding O atoms. These results correspond to the energy profiles of the pseudo-rotation of all **D** ImH_2^+, which showed the local minima at $\varphi \sim 30°$ and $\varphi \sim 250°$ and the energy barrier at $\varphi \sim 340°$, as shown in Figure 4.4(b), and indicate that the dynamics of **D** ImH_2^+ is not free rotation but stepwise orientation changes between some stable orientations on the timescale of ps. More frequent orientation changes of **D** ImH_2^+ were observed at 75 °C than at -30 °C for all geometries of **L**, **H1** and **H2**, which suggests that the experimentally observed disorder of **D** ImH_2^+ at > 70 °C is mainly because of the effect of temperature rather than because of the expansion of the space around **D** ImH_2^+ for the rotation. Unfortunately, clear correlations such as simultaneous or chained rotations could not be found between the orientation changes of the **D** ImH_2^+ ions. φ of **S** ImH_2^+ were also plotted in Figure 4.10 to investigate the dynamics of **S** ImH_2^+. While all **S** ImH_2^+ took $\varphi \sim 75°$ at -30 °C, some **S** ImH_2^+ showed orientation changes at 75 °C, though the frequencies of the orientation changes are less than those of the **D** ImH_2^+. This suggests that the **S** ImH_2^+ ions are actually dynamic rather than static at high temperature. Furthermore, in addition to the in-plane orientation change of ImH_2^+, flipping rotation were observed once for **D** ImH_2^+ and once for **S** ImH_2^+, where ImH_2^+ rotates perpendicular to the ImH_2^+ ring plane, in the $\mathbf{L_{348K}}$ MD trajectory, supposing the existence of a sufficient space for flipping rotation around **D** and **S** ImH_2^+. The results indicate that not only the in-plane orientation changes of **D** ImH_2^+ but also the orientation changes of **S** ImH_2^+ and flipping rotation of **D** and **S**

ImH_2^+, which were not observed in the experimental analysis, could occur at high temperature.

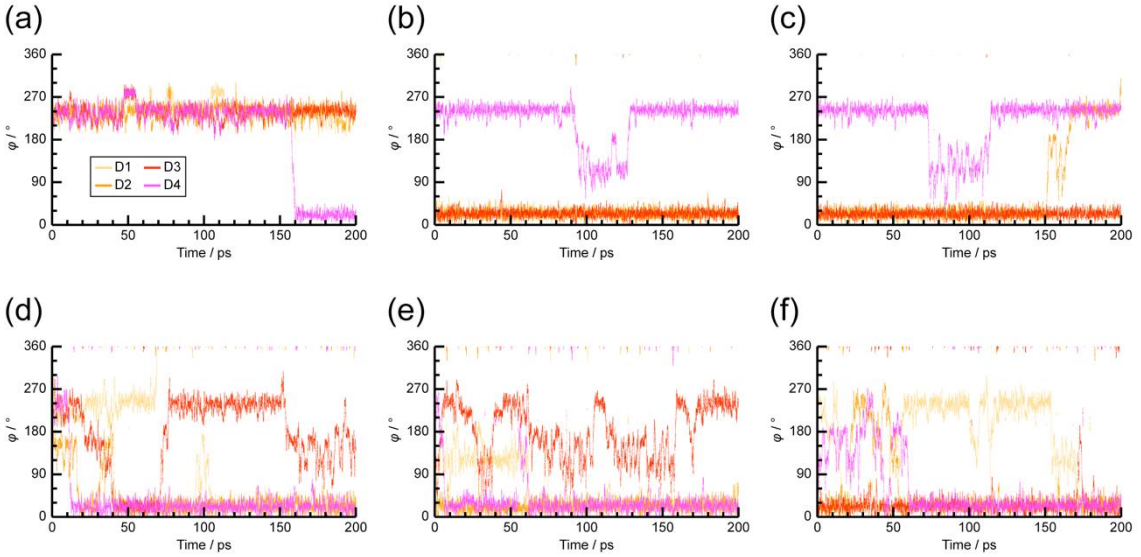

Figure 4.8. φ of each **D** ImH_2^+ of every 4 fs MD frames for 200 ps at (a) **L**$_{243K}$, (b) **H1**$_{243K}$, (c) **H2**$_{243K}$, (d) **L**$_{348K}$, (e) **H1**$_{348K}$, (f) **H2**$_{348K}$. The number of each **D** ImH_2^+ was defined in Figure 4.11.

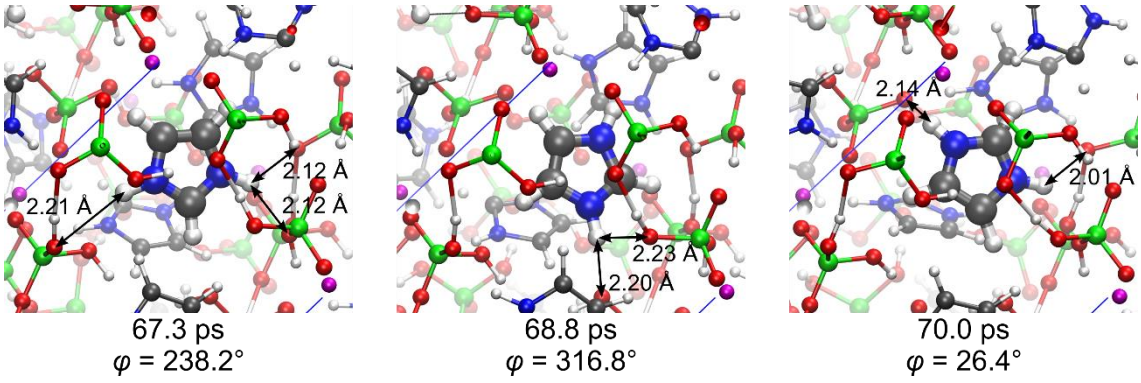

Figure 4.9. Three different orientations of **D** ImH_2^+ (D1 of Figure 4.11) and hydrogen bonds between the H atoms on the N atoms of D1 and O atoms of the phosphate groups in the MD simulation of **L**$_{348K}$. White, gray, blue, red, green and magenta spheres indicate

H, C, N, O, P and Zn atoms, respectively. D1 is emphasized with larger spheres and thicker bonds.

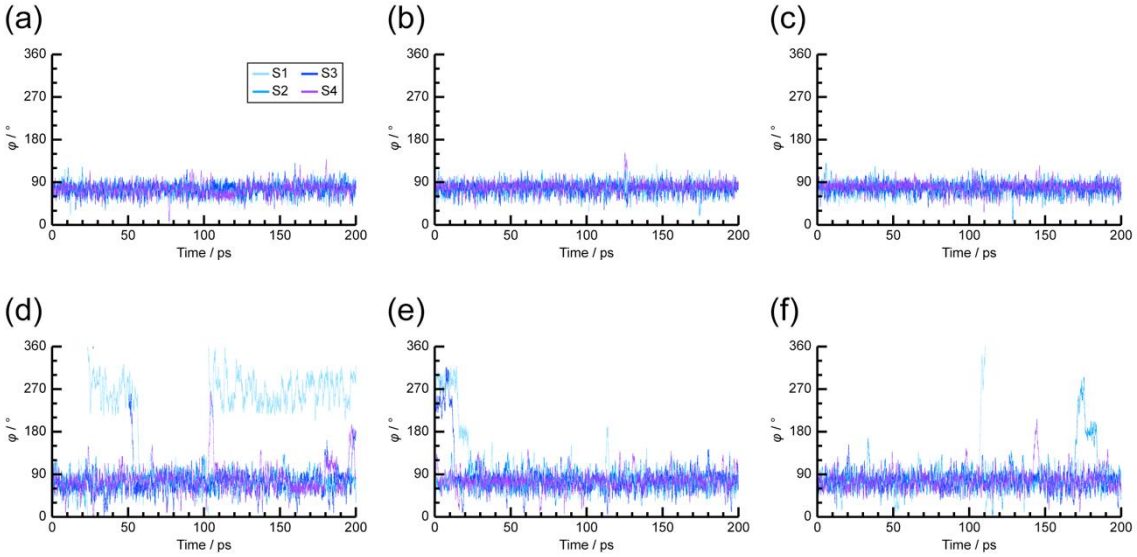

Figure 4.10. φ of each **S** ImH_2^+ of every 4 fs MD frames for 200 ps at (a) **L**$_{\mathbf{243K}}$, (b) **H1**$_{\mathbf{243K}}$, (c) **H2**$_{\mathbf{243K}}$, (d) **L**$_{\mathbf{348K}}$, (e) **H1**$_{\mathbf{348K}}$, (f) **H2**$_{\mathbf{348K}}$. The number of each **S** ImH_2^+ was defined in Figure 4.11.

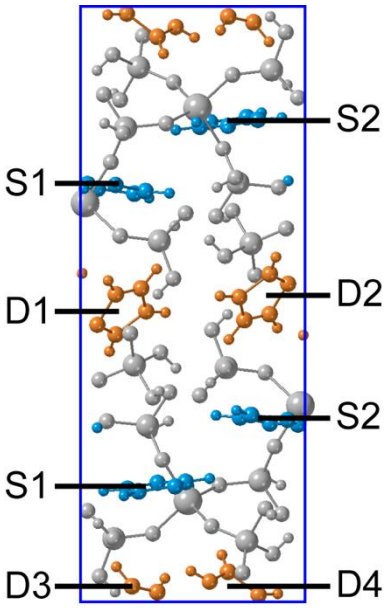

Figure 4.11. Definition of the numbers of ImH_2^+ for Figures 4.8 and 4.10. Gray, orange

and light blue spheres indicate the 1D chains in the framework, **D** ImH_2^+ ions and **S** ImH_2^+ ions, respectively.

To elucidate proton conduction pathways, the number of proton transfer in the DFTB-MD trajectories were counted. Proton transfer between phosphate groups were observed, as summarized in Table 4.4. More frequent proton transfer was observed at 75 °C than at -30 °C, indicating that higher temperature promotes proton transfer. This agrees with the experimental results showing higher conductivity at higher temperature. On the other hand, proton transfer involving neither **D** nor **S** ImH_2^+ could be observed in all MD trajectories. The reason for observing no proton transfer involving ImH_2^+ is considered to be the lower acidity of ImH_2^+ compared with the phosphate groups. As shown in the Scheme 4.1, the pK_a of ImH_2^+ (6.99 at 25 °C) is much higher than the first pK_a of H_3PO_4 (2.16 at 25 °C), which promotes proton transfer from H_3PO_4 to neutral imidazole (ImH).[114] Actually, the proton transfer from H_3PO_4 to ImH was observed while the reverse transfer was not observed in the previous Car-Parrinello MD simulations of H_3PO_4/ImH system.[115] Supposing that the phosphate groups in **CP1** show similar acidity to H_3PO_4, the phosphate groups would be much stronger acids than ImH_2^+, which prevents the proton from transferring from ImH_2^+ to phosphate groups. Relative energies of the single point calculations with DFTB vs. d_{NH} or d_{OH} were also plotted in Figure 4.12 to estimate the energy barriers of proton transfer either from ImH_2^+ to a phosphate group or between two phosphate groups. The former showed higher energy barriers than the latter, which supports the difficulty of proton transfer reactions involving ImH_2^+ in the MD simulations. The results indicate that proton conduction occurs via phosphate groups, rather than ImH_2^+.

Table 4.4. The numbers of proton transfer between the phosphate groups in MD trajectories for 200 ps at -30 °C and 75 °C. Momentary proton transfers (the proton returned within 0.1 ps after transfer) were not counted.

	Number of proton transfer	
	-30 °C	75 °C
L	22	84
H1	0	32
H2	0	42

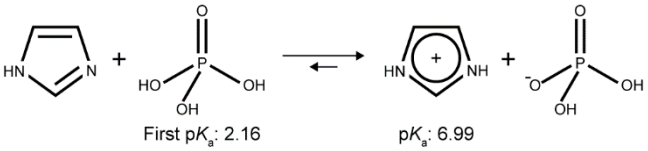

Scheme 4.1. Proton transfer reaction from H_3PO_4 to ImH and pK_a of H_3PO_4 and ImH_2^+ at 25 °C.

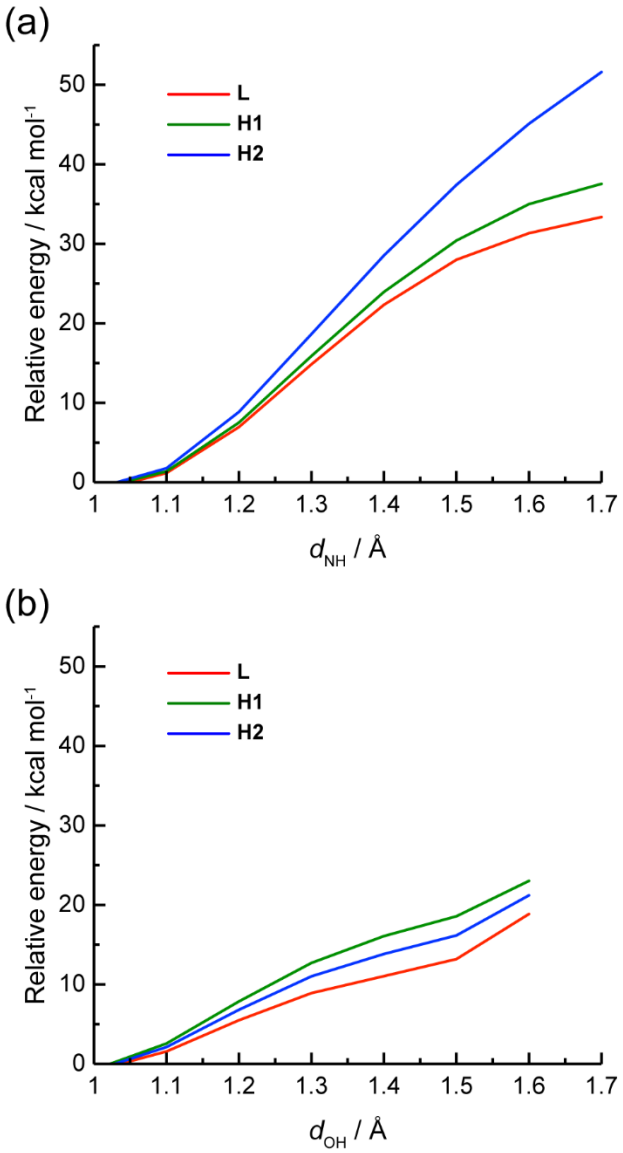

Figure 4.12. Relative energies with (a) different N-H distances of a **D** ImH_2^+ (d_{NH}) and (b) different O-H distances of a phosphate group (d_{OH}) obtained from single point calculations with DFTB to the optimized geometries with DFT, f-cell.

4.4. Conclusions

The static and dynamic properties of a 1D CP with protonated heterocycles, **CP1**, were theoretically investigated using DFT and DFTB-MD simulations. Static calculations with DFT showed that the orientations of the **D** ImH_2^+ influence the energy of the system,

through the stabilization by hydrogen bonds to the surrounding phosphate groups. Although the different energy profiles from the pseudo-rotation of one **D** ImH_2^+ and all **D** ImH_2^+ indicated the possibility that the rotational motions of **D** ImH_2^+ are correlated, such correlations have not been shown clearly in the DFTB-MD simulations. From the DFTB-MD simulations, it was revealed that the **D** ImH_2^+ ions show stepwise orientation changes between the stable orientations rather than the free rotations in the time scale of proton transfer, which is the order of ps.[116] The frequency of the orientation changes increased at higher temperature, which agreed with the experimentally observed disorder of **D** ImH_2^+. The orientation changes of **S** ImH_2^+ and flipping rotation of **D** and **S** ImH_2^+ were also observed, which were not observed in the experimental analysis. Higher frequency of the proton transfer reactions between the phosphate groups were observed at higher temperature, while the proton transfer involving ImH_2^+ was not observed, due to the lower acidity of ImH_2^+ than the phosphate groups. This indicates that the pathways of proton conduction should be on the phosphate groups, and ImH_2^+ ions do not participate in the proton conduction directly, but just stabilize the structure via hydrogen bonds. The results of this section suggest the possibility that the linkers and side phosphate ligands of CPs could play more important roles on proton conduction than the organic heterocycles, which indicates the importance to select ligands when designing CPs with higher proton conductivity. Further investigations will reveal more detailed pathways of proton conduction on the phosphate groups and the roles of the dynamics of ImH_2^+.

5. General Conclusions and Future Outlooks

In this thesis, the effects of dynamics of atoms and molecules in functional materials on the functions are elucidated using theoretical calculations with semi-empirical DFTB method. In Section 2, DFTB-MD simulation of a double-helical molecule, BBDD, were performed revealing that the exchange following disentanglement is essential for the stepwise helix-inversion process. This indicates the importance of tuning terminal groups to design double-helical molecules. In Section 3, various monolayer and layered structures of a double stage 2D COF was investigated using DFTB. The rotation of the *p*-phenylene rings makes an influence on the global stacking orders. The discrepancy between the powder XRD pattern of the most stable stacked structure and the experimental one indicates that the dynamics is important for the self-assembly process to form the COF. In Section 4 static DFT calculations and dynamic DFTB-MD simulations of a proton-conductive 1D CP including ImH_2^+ were carried out. The orientations of ImH_2^+ affects the stabilization of the whole system, while the proton transfer reactions were limited between the phosphate groups, not involving ImH_2^+. It is supposed that the proton conduction pathway of the CP is on the phosphate groups and ImH_2^+ groups stabilize the system.

As a summary, this thesis showed that both of local and global dynamics can affect expression of the functions of the materials, and those dynamics could influence each other. The importance of considering such dynamics to design functional materials was exhibited. This thesis also showed the effectiveness of theoretical calculations of structures, properties and dynamics of atoms and molecules for elucidation of dynamic mechanisms of functions of materials, which are difficult to investigate with experimental approaches.

As a future outlook, the role of computational chemistry on development of functional materials will increase more and more with performance improvement of computers and development of efficient computational methods with higher accuracy or higher efficiency, or both.

Acknowledgements

The present work was performed under the supervision of Prof. Stephan Irle in Oak Ridge National Laboratory, and Prof. Takeshi Yanai in Nagoya University. The author gives maximal compliment to them.

Foremost, the author expresses the largest gratitude to Assoc. Prof. Yuh Hijikata in Hokkaido University, who not only discussed and advised to the research but also revised this thesis after the author left the university.

The author is deeply grateful to Assoc. Prof. Daisuke Yokogawa in the University of Tokyo for fruitful discussions and technical supports.

The author would like to thank all current and previous members and staffs of Quantum Chemistry Laboratory and Institute of Transformative Bio-Molecules (ITbM). They give the author various supports and knowledge and the fulfilling research life.

The author expresses special thanks to Prof. Eiji Yashima in Nagoya University, Prof. Donglin Jiang in National University of Singapore, Assoc. Prof. Alister Page in the University of Newcastle and Prof. Hiromi Nakai in Waseda University for their help, advice and discussions about the researches. The author will also thanks to the group members of Assoc. Prof. Page, who supported the author's stay in Australia.

The author also appreciates the bosses and co-workers in Meitetsucom Co. Ltd., who allowed the author writing this thesis while working at the company.

Finally, the author thanks my family so much for all of their supports.

References

1. Yashima, E., Ousaka, N., Taura, D., Shimomura, K., Ikai, T., Maeda, K. *Chemical Reviews* **2016**, 116, 13752-13990.
2. Paddison, S. J. *Annual Review of Materials Research* **2003**, 33, 289-319.
3. Jorn, R., Savage, J., Voth, G. A. *Accounts of Chemical Research* **2012**, 45, 2002-2010.
4. Steele, B. C. H., Heinzel, A. *Nature* **2001**, 414, 345.
5. Hamrock, S. J., Yandrasits, M. A. *Journal of Macromolecular Science, Part C* **2006**, 46, 219-244.
6. Devanathan, R. *Energy & Environmental Science* **2008**, 1, 101-119.
7. Hickner, M. A., Ghassemi, H., Kim, Y. S., Einsla, B. R., McGrath, J. E. *Chemical Reviews* **2004**, 104, 4587-4612.
8. Rubatat, L., Gebel, G., Diat, O. *Macromolecules* **2004**, 37, 7772-7783.
9. Gebel, G., Diat, O. *Fuel Cells* **2005**, 5, 261-276.
10. Cappadonia, M., Erning, J. W., Niaki, S. M. S., Stimming, U. *Solid State Ionics* **1995**, 77, 65-69.
11. Choe, Y.-K., Tsuchida, E., Ikeshoji, T., Yamakawa, S., Hyodo, S.-a. *Physical Chemistry Chemical Physics* **2009**, 11, 3892-3899.
12. Draber, F. M., Ader, C., Arnold, J. P., Eisele, S., Grieshammer, S., Yamaguchi, S., Martin, M. *Nature Materials* **2020**, 19, 338-346.
13. Kusoglu, A., Weber, A. Z. *Chemical Reviews* **2017**, 117, 987-1104.
14. 岡崎, 進., 吉井, 範. コンピュータ・シミュレーションの基礎 (第 2 版); 化学同人: 京都, 2013.

15. Alder, B. J., Wainwright, T. E. *The Journal of Chemical Physics* **1959**, 31, 459-466.

16. Car, R., Parrinello, M. *Physical Review Letters* **1985**, 55, 2471-2474.

17. 常田, 貴. 密度汎関数法の基礎; 講談社: 東京, 2012.

18. Sholl, D. S. S., Janice A. Density Functional Theory A Practical Introduction; 吉岡書店: 京都, 2014.

19. Elstner, M., Porezag, D., Jungnickel, G., Elsner, J., Haugk, M., Frauenheim, T., Suhai, S., Seifert, G. *Physical Review B* **1998**, 58, 7260-7268.

20. Yang, Yu, H., York, D., Cui, Q., Elstner, M. *The Journal of Physical Chemistry A* **2007**, 111, 10861-10873.

21. Gaus, M., Cui, Q., Elstner, M. *Journal of Chemical Theory and Computation* **2011**, 7, 931-948.

22. Gaus, M., Cui, Q., Elstner, M. *Wiley Interdisciplinary Reviews: Computational Molecular Science* **2013**, 4, 49-61.

23. Elstner, M., Seifert, G. *Philosophical Transactions of the Royal Society A: Mathematical, Physical and Engineering Sciences* **2014**, 372.

24. Řezáč, J. *Journal of Chemical Theory and Computation* **2017**, 13, 4804-4817.

25. Watson, J. D., Crick, F. H. C. *Nature* **1953**, 171, 737.

26. Travers, A., Muskhelishvili, G. *The FEBS Journal* **2015**, 282, 2279-2295.

27. Yashima, E., Maeda, K., Iida, H., Furusho, Y., Nagai, K. *Chemical Reviews* **2009**, 109, 6102-6211.

28. Iida, H., Ohmura, K., Noda, R., Iwahana, S., Katagiri, H., Ousaka, N., Hayashi,

T., Hijikata, Y., Irle, S., Yashima, E. *Chemistry – An Asian Journal* **2017**, 12, 927-935.

29. Côté, A. P., Benin, A. I., Ockwig, N. W., O'Keeffe, M., Matzger, A. J., Yaghi, O. M. *Science* **2005**, 310, 1166-1170.
30. Feng, X., Ding, X., Jiang, D. *Chemical Society Reviews* **2012**, 41, 6010-6022.
31. Waller, P. J., Gandara, F., Yaghi, O. M. *Accounts of Chemical Research* **2015**, 48, 3053-3063.
32. Beaudoin, D., Maris, T., Wuest, J. D. *Nature Chemistry* **2013**, 5, 830-834.
33. Zhang, Y. B., Su, J., Furukawa, H., Yun, Y., Gandara, F., Duong, A., Zou, X., Yaghi, O. M. *Journal of the American Chemical Society* **2013**, 135, 16336-16339.
34. Ascherl, L., Sick, T., Margraf, J. T., Lapidus, S. H., Calik, M., Hettstedt, C., Karaghiosoff, K., Döblinger, M., Clark, T., Chapman, K. W., Auras, F., Bein, T. *Nature Chemistry* **2016**, 8, 310-316.
35. Horike, S., Umeyama, D., Inukai, M., Itakura, T., Kitagawa, S. *Journal of the American Chemical Society* **2012**, 134, 7612-7615.
36. Lehn, J. M., Rigault, A., Siegel, J., Harrowfield, J., Chevrier, B., Moras, D. *Proceedings of the National Academy of Sciences of the United States of America* **1987**, 84, 2565.
37. Albrecht, M. *Chemical Reviews* **2001**, 101, 3457-3498.
38. Huc, I. *European Journal of Organic Chemistry* **2003**, 2004, 17-29.
39. Tanaka, Y., Katagiri, H., Furusho, Y., Yashima, E. *Angewandte Chemie International Edition* **2005**, 44, 3867-3870.
40. Tashiro, R., Sugiyama, H. *Journal of the American Chemical Society* **2005**, 127, 2094-2097.

41. Hasegawa, T., Furusho, Y., Katagiri, H., Yashima, E. *Angewandte Chemie International Edition* **2007**, 46, 5885-5888.

42. Amemiya, R., Yamaguchi, M. *Organic & Biomolecular Chemistry* **2008**, 6, 26-35.

43. Ito, H., Furusho, Y., Hasegawa, T., Yashima, E. *Journal of the American Chemical Society* **2008**, 130, 14008-14015.

44. Bezer, S., Rapireddy, S., Skorik, Y. A., Ly, D. H., Achim, C. *Inorganic Chemistry* **2011**, 50, 11929-11937.

45. Yamada, H., Wu, Z.-Q., Furusho, Y., Yashima, E. *Journal of the American Chemical Society* **2012**, 134, 9506-9520.

46. Rich, A., Nordheim, A., Wang, A. H. J. *Annual Review of Biochemistry* **1984**, 53, 791-846.

47. Fujiki, M. *Journal of the American Chemical Society* **2000**, 122, 3336-3343.

48. Fujiki, M. *Journal of Organometallic Chemistry* **2003**, 685, 15-34.

49. Tang, K., Green, M. M., Cheon, K. S., Selinger, J. V., Garetz, B. A. *Journal of the American Chemical Society* **2003**, 125, 7313-7323.

50. Zhao, H., Sanda, F., Masuda, T. *Macromolecular Chemistry and Physics* **2005**, 206, 1653-1658.

51. Sakurai, S.-i., Okoshi, K., Kumaki, J., Yashima, E. *Journal of the American Chemical Society* **2006**, 128, 5650-5651.

52. Kersting, B., Meyer, M., Powers, R. E., Raymond, K. N. *Journal of the American Chemical Society* **1996**, 118, 7221-7222.

53. Albrecht, M., Schneider, M. *Chemical Communications* **1998**, 137-138.

54. Charbonnière, L. J., Williams, A. F., Frey, U., Merbach, A. E., Kamalaprija, P.,

Schaad, O. *Journal of the American Chemical Society* **1997**, 119, 2488-2496.

55. TURBOMOLE V6.6 **2014**, a development of University of Karlsruhe and Forschungszentrum Karlsruhe GmbH, 1989-2007, TURBOMOLE GmbH, since 2007; available from http://www.turbomole.com.

56. Eichkorn, K., Treutler, O., Öhm, H., Häser, M., Ahlrichs, R. *Chemical Physics Letters* **1995**, 242, 652-660.

57. Dirac, P. A. M. *Proceedings of the Royal Society of London. Series A* **1929**, 123, 714.

58. Slater, J. C. *Physical Review* **1951**, 81, 385-390.

59. Perdew, J. P., Wang, Y. *Physical Review B* **1992**, 45, 13244-13249.

60. Tao, J., Perdew, J. P., Staroverov, V. N., Scuseria, G. E. *Physical Review Letters* **2003**, 91, 146401.

61. Aradi, B., Hourahine, B., Frauenheim, T. *The Journal of Physical Chemistry A* **2007**, 111, 5678-5684.

62. J. Frenzel, A. F. O., N. Jardillier, T. Heine, G. Seifert. *TU--Dresden 2004--2009*.

63. Lukose, B., Kuc, A., Frenzel, J., Heine, T. *Beilstein Journal of Nanotechnology* **2010**, 1, 60-70.

64. Rappe, A. K., Casewit, C. J., Colwell, K. S., Goddard, W. A., Skiff, W. M. *Journal of the American Chemical Society* **1992**, 114, 10024-10035.

65. Zhechkov, L., Heine, T., Patchkovskii, S., Seifert, G., Duarte, H. A. *Journal of Chemical Theory and Computation* **2005**, 1, 841-847.

66. Kumar, S., Rosenberg, J. M., Bouzida, D., Swendsen, R. H., Kollman, P. A. *Journal of Computational Chemistry* **1995**, 16, 1339-1350.

67. Grossfield, A. In "WHAM: the weighted histogram analysis method", version

2.0.9, http://membrane.urmc.rochester.edu/content/wham.

68. Davis, M. E. *Nature* **2002**, 417, 813-821.

69. Kitagawa, S., Kitaura, R., Noro, S.-i. *Angewandte Chemie International Edition* **2004**, 43, 2334-2375.

70. Chandra, S., Kundu, T., Kandambeth, S., Babarao, R., Marathe, Y., Kunjir, S. M., Banerjee, R. *Journal of the American Chemical Society* **2014**, 136, 6570-6573.

71. Côté, A. P., El-Kaderi, H. M., Furukawa, H., Hunt, J. R., Yaghi, O. M. *Journal of the American Chemical Society* **2007**, 129, 12914-12915.

72. Furukawa, H., Yaghi, O. M. *Journal of the American Chemical Society* **2009**, 131, 8875-8883.

73. Ding, S. Y., Gao, J., Wang, Q., Zhang, Y., Song, W. G., Su, C. Y., Wang, W. *Journal of the American Chemical Society* **2011**, 133, 19816-19822.

74. Dogru, M., Bein, T. *Chemical Communications (Cambridge)* **2014**, 50, 5531-5546.

75. Bunck, D. N., Dichtel, W. R. *Angewandte Chemie International Edition* **2012**, 51, 1885-1889.

76. Jin, S., Supur, M., Addicoat, M., Furukawa, K., Chen, L., Nakamura, T., Fukuzumi, S., Irle, S., Jiang, D. *Journal of the American Chemical Society* **2015**, 137, 7817-7827.

77. Hu, Z., Zhang, L., Jiang, J. *Journal of Chemical Physics* **2012**, 136, 244703.

78. Cravillon, J., Nayuk, R., Springer, S., Feldhoff, A., Huber, K., Wiebcke, M. *Chemistry of Materials* **2011**, 23, 2130-2141.

79. Rietveld, H. *Acta Crystallographica* **1967**, 22, 151-152.

80. Rabbani, M. G., Sekizkardes, A. K., Kahveci, Z., Reich, T. E., Ding, R., El-Kaderi, H. M. *Chemistry* **2013**, 19, 3324-3328.

81. McCusker, L. B., Von Dreele, R. B., Cox, D. E., Louer, D., Scardi, P. *Journal of Applied Crystallography* **1999**, 32, 36-50.

82. Chen, X., Addicoat, M., Jin, E., Xu, H., Hayashi, T., Xu, F., Huang, N., Irle, S., Jiang, D. *Scientific Reports* **2015**, 5, 14650.

83. Grundkötter-Stock, B., Bezugly, V., Kunstmann, J., Cuniberti, G., Frauenheim, T., Niehaus, T. A. *Journal of Chemical Theory and Computation* **2012**, 8, 1153-1163.

84. Moreira, N. H., Dolgonos, G., Aradi, B., da Rosa, A. L., Frauenheim, T. *Journal of Chemical Theory and Computation* **2009**, 5, 605-614.

85. https://www.dftb.org/.

86. Perdew, J. P., Burke, K., Ernzerhof, M. *Physical Review Letters* **1996**, 77, 3865-3868.

87. Grimme, S. *Journal of Computational Chemistry* **2006**, 27, 1787-1799.

88. Kresse, G., Hafner, J. *Physical Review B* **1993**, 47, 558-561.

89. Kresse, G., Hafner, J. *Physical Review B* **1994**, 49, 14251-14269.

90. Kresse, G., Furthmüller, J. *Computational Materials Science* **1996**, 6, 15-50.

91. Kresse, G., Furthmüller, J. *Physical Review B* **1996**, 54, 11169-11186.

92. Gaussian 03, Revision E.01, Frisch, M. J., Trucks, G. W., Schlegel, H. B., Scuseria, G. E., Robb, M. A., Cheeseman, J. R., Montgomery, Jr., J. A., Vreven, T., Kudin, K. N., Burant, J. C., Millam, J. M., Iyengar, S. S., Tomasi, J., Barone, V., Mennucci, B., Cossi, M., Scalmani, G., Rega, N., Petersson, G. A., Nakatsuji, H., Hada, M., Ehara, M., Toyota, K., Fukuda, R., Hasegawa, J., Ishida, M., Nakajima, T., Honda, Y., Kitao, O., Nakai, H., Klene, M., Li, X., Knox, J. E., Hratchian, H. P., Cross, J. B., Bakken, V., Adamo, C., Jaramillo, J., Gomperts, R., Stratmann, R. E., Yazyev, O., Austin, A. J., Cammi, R., Pomelli, C., Ochterski, J. W., Ayala, P. Y., Morokuma,

K., Voth, G. A., Salvador, P., Dannenberg, J. J., Zakrzewski, V. G., Dapprich, S., Daniels, A. D., Strain, M. C., Farkas, O., Malick, D. K., Rabuck, A. D., Raghavachari, K., Foresman, J. B., Ortiz, J. V., Cui, Q., Baboul, A. G., Clifford, S., Cioslowski, J., Stefanov, B. B., Liu, G., Liashenko, A., Piskorz, P., Komaromi, I., Martin, R. L., Fox, D. J., Keith, T., Al-Laham, M. A., Peng, C. Y., Nanayakkara, A., Challacombe, M., Gill, P. M. W., Johnson, B., Chen, W., Wong, M. W., Gonzalez, C., Pople, J. A.; Gaussian, Inc., Wallingford CT, **2004**.

93. Gaussian 09, Revision D.01, Frisch, M. J., Trucks, G. W., Schlegel, H. B., Scuseria, G. E., Robb, M. A., Cheeseman, J. R., Scalmani, G., Barone, V., Mennucci, B., Petersson, G. A., Nakatsuji, H., Caricato, M., Li, X., Hratchian, H. P., Izmaylov, A. F., Bloino, J., Zheng, G., Sonnenberg, J. L., Hada, M., Ehara, M., Toyota, K., Fukuda, R., Hasegawa, J., Ishida, M., Nakajima, T., Honda, Y., Kitao, O., Nakai, H., Vreven, T., Montgomery, Jr., J. A., Peralta, J. E., Ogliaro, F., Bearpark, M., Heyd, J. J., Brothers, E., Kudin, K. N., Staroverov, V. N., Kobayashi, R., Normand, J., Raghavachari, K., Rendell, A., Burant, J. C., Iyengar, S. S., Tomasi, J., Cossi, M., Rega, N., Millam, J. M., Klene, M., Knox, J. E., Cross, J. B., Bakken, V., Adamo, C., Jaramillo, J., Gomperts, R., Stratmann, R. E., Yazyev, O., Austin, A. J., Cammi, R., Pomelli, C., Ochterski, J. W., Martin, R. L., Morokuma, K., Zakrzewski, V. G., Voth, G. A., Salvador, P., Dannenberg, J. J., Dapprich, S., Daniels, A. D., Farkas, Ö., Foresman, J. B., Ortiz, J. V., Cioslowski, J., Fox, D. J., Gaussian, Inc., Wallingford CT, **2009**.

94. Nishizawa, H., Nishimura, Y., Kobayashi, M., Irle, S., Nakai, H. *Journal of Computational Chemistry* **2016**, 37, 1983-1992.

95. Chu, S., Cui, Y., Liu, N. *Nature Materials* **2016**, 16, 16.

96. Horike, S., Umeyama, D., Kitagawa, S. *Accounts of Chemical Research* **2013**, 46, 2376-2384.

97. Meng, X., Wang, H.-N., Song, S.-Y., Zhang, H.-J. *Chemical Society Reviews* **2017**, 46, 464-480.

98. Nagao, Y., Ikeda, R., Kanda, S., Kubozono, Y., Kitagawa, H. *Molecular Crystals and Liquid Crystals* **2002**, 379, 89-94.

99. Bureekaew, S., Horike, S., Higuchi, M., Mizuno, M., Kawamura, T., Tanaka, D., Yanai, N., Kitagawa, S. *Nature Materials* **2009**, 8, 831.

100. Wei, Y.-S., Hu, X.-P., Han, Z., Dong, X.-Y., Zang, S.-Q., Mak, T. C. W. *Journal of the American Chemical Society* **2017**, 139, 3505-3512.

101. Umeyama, D., Horike, S., Inukai, M., Itakura, T., Kitagawa, S. *Journal of the American Chemical Society* **2012**, 134, 12780-12785.

102. Ramaswamy, P., Wong, N. E., Shimizu, G. K. H. *Chemical Society Reviews* **2014**, 43, 5913-5932.

103. Bauer, F., Denneler, S., Willert-Porada, M. *Journal of Polymer Science Part B: Polymer Physics* **2005**, 43, 786-795.

104. Rozière, J., Jones, D. J. *Annual Review of Materials Research* **2003**, 33, 503-555.

105. Giannozzi, P., Baroni, S., Bonini, N., Calandra, M., Car, R., Cavazzoni, C., Ceresoli, D., Chiarotti, G. L., Cococcioni, M., Dabo, I., Dal Corso, A., de Gironcoli, S., Fabris, S., Fratesi, G., Gebauer, R., Gerstmann, U., Gougoussis, C., Kokalj, A., Lazzeri, M., Martin-Samos, L., Marzari, N., Mauri, F., Mazzarello, R., Paolini, S., Pasquarello, A., Paulatto, L., Sbraccia, C., Scandolo, S., Sclauzero, G., Seitsonen, A. P., Smogunov, A., Umari, P., Wentzcovitch, R. M. *Journal of Physics: Condensed Matter* **2009**, 21, 395502.

106. Giannozzi, P., Andreussi, O., Brumme, T., Bunau, O., Buongiorno Nardelli, M., Calandra, M., Car, R., Cavazzoni, C., Ceresoli, D., Cococcioni, M., Colonna, N., Carnimeo, I., Dal Corso, A., de Gironcoli, S., Delugas, P., DiStasio, R. A., Ferretti, A., Floris, A., Fratesi, G., Fugallo, G., Gebauer, R., Gerstmann, U., Giustino, F., Gorni, T., Jia, J., Kawamura, M., Ko, H. Y., Kokalj, A., Küçükbenli, E., Lazzeri, M., Marsili, M., Marzari, N., Mauri, F., Nguyen, N. L., Nguyen, H. V., Otero-de-la-Roza, A., Paulatto, L., Poncé, S., Rocca, D., Sabatini, R., Santra, B., Schlipf, M., Seitsonen, A. P., Smogunov, A., Timrov, I., Thonhauser, T., Umari, P., Vast, N., Wu, X., Baroni, S. *Journal of Physics: Condensed Matter* **2017**, 29, 465901.

107. Dal Corso, A. *Computational Materials Science* **2014**, 95, 337-350.

108. https://dalcorso.github.io/pslibrary/.

109. Gaus, M., Goez, A., Elstner, M. *Journal of Chemical Theory and Computation* **2013**, 9, 338-354.

110. Gaus, M., Lu, X., Elstner, M., Cui, Q. *Journal of Chemical Theory and Computation* **2014**, 10, 1518-1537.

111. Lu, X., Gaus, M., Elstner, M., Cui, Q. *The Journal of Physical Chemistry B* **2015**, 119, 1062-1082.

112. Grimme, S., Antony, J., Ehrlich, S., Krieg, H. *The Journal of Chemical Physics* **2010**, 132, 154104.

113. Kollipost, F., Andersen, J., Mahler, D. W., Heimdal, J., Heger, M., Suhm, M. A., Larsen, R. W. *The Journal of Chemical Physics* **2014**, 141, 174314.

114. Haynes, W. M., Lide, D. R., Bruno, T. J. CRC Handbook of Chemistry and Physics, 97th Edition; CRC Press: Boca Raton, 2016.

115. Vilčiauskas, L., Tuckerman, M. E., Melchior, J. P., Bester, G., Kreuer, K.-D. *Solid*

State Ionics **2013**, 252, 34-39.

116. Vilčiauskas, L., Tuckerman, M. E., Bester, G., Paddison, S. J., Kreuer, K.-D. *Nature Chemistry* **2012**, 4, 461-466.

List of Publications

Sub-theses

1. Hayashi, T., Hijikata, Y., Page, A., Jiang, D., Irle, S. *Chemical Physics Letters* **2016**, 664, 101-107
2. Hayashi, T., Lee, K. H., Iida, H., Yashima, E., Irle, S., Hijikata, Y. *Journal of Computational Chemistry* **2019**, 40, 2036-2042

Reference Theses

1. Chen, X., Addicoat, M., Jin, E., Xu, H., Hayashi, T., Xu, F., Huang, N., Irle, S., Jiang, D. *Scientific Reports* **2015**, 5, 14650
2. Iida, H., Ohmura, K., Noda, R., Iwahana, S., Katagiri, H., Ousaka, N., Hayashi, T., Hijikata, Y., Irle, S., Yashima, E. *Chemistry – An Asian Journal* **2017**, 12, 927-935.
3. Kundu, S. K., Singuru, R., Hayashi, T., Hijikata, Y., Irle, S., Mondal, J. *ChemistrySelect* **2017**, 2, 4705-4716
4. Bhanja, P., Das, S. K., Bhunia, K., Pradhan, D., Hayashi, T., Hijikata, Y., Irle, S., Bhaumik, A. *ACS Sustainable Chemistry & Engineering* **2018**, 6, 202-209
5. Mondal, S., Singuru, R., Shit, S. C., Hayashi, T., Irle, S., Hijikata, Y., Mondal, J. Bhaumik, A. *ACS Sustainable Chemistry & Engineering* **2018**, 6, 1610-1619